

**Author**

Carl E. Henderson

**Title**

Protocols and Pitfalls of Electron Microprobe Analysis of Apatite

Submitted for Publication in:

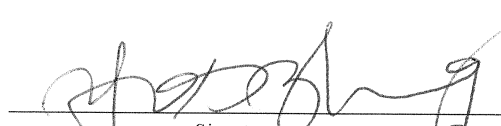

*The American Mineralogist*

in lieu of thesis in partial fulfillment of the requirements for the degree of

**Master of Science in Geology**

Department of Geological Sciences

The University of Michigan

 Signature	Accepted by: <u>          Youxue Zhang          </u> Name	<u>          25 April 2011          </u> Date
 Signature	<u>          Rodney C. Ewing          </u> Name	<u>          19 April 2011          </u> Date
<u>          Rebecca Lange          </u> Department Chair Signature	<u>          Rebecca Lange          </u> Name	<u>          25 April 2011          </u> Date

I hereby grant the University of Michigan, its heirs and assigns, the non-exclusive right to reproduce and distribute single copies of my thesis, in whole or in part, in any format. I represent and warrant to the University of Michigan that the thesis is an original work, does not infringe or violate any rights of others, and that I make these grants as the sole owner of the rights to my thesis. I understand that I will not receive royalties for any reproduction of this thesis.

- Permission granted.
- Permission granted to copy after: \_\_\_\_\_
- Permission declined.

          Carl Henderson            
Author Signature



## ABSTRACT

A suite of oriented apatite samples, including the well-known Durango (Mexico) and Wilberforce (Canada) apatites, was used to evaluate optimal analytical conditions for electron microprobe analysis (EMPA) of apatite. X-ray count rates as a function of beam exposure time were acquired for a variety of electron beam settings, in order to select beam conditions yielding stable or predictably varying count rates. However, significant anisotropy in the F count rate due to sample orientation resulted in overestimation of F concentrations on samples analyzed with the crystallographic **c**-axis parallel to the electron beam, even when careful zero time count rate extrapolation routines were used. Other techniques, such as cryogenic cooling, use of Al and Au conductive coatings and sample motion during analysis were also evaluated. A second suite of synthetic apatites (Schettler et al. 2011; provided by D. Harlov) of known composition was analyzed to confirm accuracy of the analytical procedure. BSE, CL and X-ray images of many of the apatite samples show elemental zoning, which may affect their use as primary microanalysis standards. Evaluation of the results indicates that F (and other elements) in apatite can be analyzed accurately by electron microprobe under any of the following three sets of conditions: (i) apatite crystals where the orientation of the electron beam is perpendicular to the **c**-axis of the crystal and use of a defocused or rastered beam of  $\geq 5 \mu\text{m}$  diameter; (ii) use of sample motion at a velocity of  $\geq 5 \mu\text{m/s}$  with a defocused or rastered beam of  $\geq 5 \mu\text{m}$  diameter on a large, homogenous apatite grain; and (iii) use of cryogenic cooling of the sample to about  $-80^\circ\text{C}$  with a rastered or defocused beam and an extrapolated time zero F counting rate. Quantitative results from the oriented apatites allowed calculation of (OH) contents, which were in good agreement with direct IR measurements.

**Keywords:** Apatite, electron probe microanalysis, standards

## INTRODUCTION

Apatite,  $\text{Ca}_5(\text{PO}_4)_3(\text{F},\text{Cl},\text{OH})$ , or more generally  $\text{M}_5(\text{ZO}_4)_3\text{X}$ , is a ubiquitous accessory mineral found in a wide variety of earth materials. Its composition contains a wealth of petrologic information, especially for understanding volatile and fluid compositions during crystallization. Quantitative analysis of apatite by electron microprobe analysis (EMPA) is problematic due to electron beam sensitivity and crystallographic orientation effects, especially with regards to F concentration (Stormer et al. 1993; Pyle et al. 2002). However, accurate F and Cl measurements are necessary for estimating the OH component of the X-site anions, assuming no other X-site substitutions, since H cannot be directly determined by EMPA. This study sets out to design an accurate and self-consistent analytical protocol which can be used to analyze a wide range of apatite compositions. FTIR spectroscopy methods to determine OH directly are used as a crosscheck on the calculated OH values from the EMPA results.

Stormer et al. (1993) noted variations in apatite F X-ray emission with beam exposure time. They identified beam current and spot size as the major controlling factors of count rate variation, but also demonstrated the significant effect of crystallographic orientation on F, and to a lesser extent, Cl, Ca, and P X-ray count rates. Samples of Durango apatite (Cerro de Mercado, Durango, Mexico) analyzed at typical electron beam conditions with the beam parallel to the crystallographic **c**-axis showed rapid increases in F emission during the first 60-120 s, while samples oriented with the beam perpendicular to the **c**-axis showed slower increases. After an initial rise, the F count rates decreased to values equal to or lower than their zero time values.

Stormer et al. (1993) also noted that the effect was permanent and could not be reversed by blanking the electron beam for short or long periods during analysis. Ca and P count rates showed a change inversely proportional to the F count rate, though the change was small (a few percent relative) and might not be noticed during short duration analyses. The effect of beam voltage was also studied, and was determined to be negligible on the initial rate F rate at beam voltages between 7 and 15 kV. They deduced that raising beam voltage would lead to an increased electron penetration depth and, thus, a decrease in the electrical gradient presumed to drive the F count rate increase. However, raising voltage could also bring a concurrent increase of the volume from which F anions could diffuse and negate the benefit of a lowered electrical gradient. Stormer and Pierson (1993) tested Wilberforce apatite, an end-member fluorapatite, and noted that its F anisotropy was also strong, even on sections prepared with the **c**-axis oriented as much as 46° from the electron beam axis.

Pyle et al. (2002) suggested an analytical sequence whereby the major elements (Ca, P, F, Cl) were analyzed with short counting times at the beginning of the analytical sequence. After collection of data for the major elements, longer measurements were made for the minor and trace elements, since this second group of elements shows less variation with beam exposure time.

Webster et al. (2009) performed quantitative analysis on a series of apatites equilibrated in hydrothermal experiments involving silicate melts, using a 15 kV, 10 nA, defocused beam (6-20 μm in diameter), while moving the sample during analysis, and did not see a difference in F concentration between sample orientations.

Adams et al. (2010) reproduced the experiments of Stormer et al. (1993) on oriented samples of Durango apatite over a range of beam currents from 4 to 50 nA and beam spot sizes of 1 to 20  $\mu\text{m}$  with long duration beam exposures of almost one hour. They noted that software extrapolation of the F count rate to a zero time value, using time-dependent intensity (TDI) curves, could be reliably used to calculate F concentrations, except in the case where the electron beam was parallel or nearly parallel to the apatite c-axis and with the extreme conditions of either a 1  $\mu\text{m}$  spot size or a 50 nA beam current.

McCubbin et al. (2010) used a 15 kV and 25 nA beam with spot sizes ranging from 2-20  $\mu\text{m}$  in diameter for their measurements on lunar apatites. They also used TDI corrections acquired over the first  $\sim 125$  s of each analysis to back-calculate an initial F intensity. Analyses where the TDI curves were non-linear or had a negative slope were discarded. They were unable to correlate TDI slope with grain orientation, as determined by crystal morphology.

Many other geological materials, including natural glasses, feldspars, and carbonates show electron beam-induced damage or X-ray count rate temporal variation. A variety of analytical methods have been used to minimize these effects. The first line of defense in mitigating beam damage usually involves lowering beam current density by some combination of increased spot size and decreased beam current (e.g., Morgan and London 1996, 2005). If plots of X-ray count rate versus beam exposure time show a predictable variation in X-ray signal, then it may be possible to extrapolate the count rate back to a zero time rate (Nielsen and Sigurdsson 1981; Devine et al. 1995). Other techniques to slow or prevent beam damage or element migration include cryogenic sample cooling (Nielsen and Sigurdsson 1980; Kearns et al. 2002), application of alternative metal

coatings such as Ag, Al or Au (Smith 1986; Jercinovic et al. 2005), or sample movement to expose fresh surfaces during the course of the analysis. In this study, these methods were evaluated on oriented apatite samples to see if F (and Cl) X-ray variations with time or orientation could be eliminated or controlled.

## **ANALYTICAL METHODS**

Wafers approximately 2 mm thick and sliced perpendicularly to the **c**-axis were cut from gem-quality samples of apatite from the well-known localities of Cerro de Mercado, Durango, Mexico and Wilberforce, Ontario, Canada. Additional oriented samples from Silver Crater Mine, Ontario (a fluorapatite, designated “SCM”), High Atlas Mountains, Morocco (an intermediate F-OH-Cl apatite, designated “HAM”) from a gem dealer, a sample purchased from an online gem dealer (an intermediate F-OH apatite, designated “Gem3”) and another large specimen labeled "Asparagus Stone" (presumably Durango apatite) from the University of Michigan mineral collection were also prepared in the same manner. The cut samples were mounted in two orientations: one with the (001) plane perpendicular to the polished surface of the mount (crystallographic **c**-axis perpendicular to the electron beam) and one with the (001) plane parallel to the surface (crystallographic **c**-axis parallel to the electron beam). The samples were mounted in epoxy resin, polished using standard preparation techniques, and coated with approximately 15 nm of carbon by thermal evaporation, as estimated by the method of Kerrick et al. (1973). Non-oriented grains of a synthetic end-member chlorapatite (synthesized by S. Prowatke, provided by Z. Sharp, and assumed stoichiometric),

synthetic  $\text{MgF}_2$ , a natural fluortopaz (Topaz Mountain, Utah) and a natural fluorite (unknown locality) were prepared in a like manner for evaluation as analytical standards.

Most of the work in this study was performed on a CAMECA SX-100 electron microprobe analyzer controlled by CAMECA PeakSight software. W-Si layered-dispersion elements (LDEs), also known as pseudo-crystals (PCs), with d-spacings of  $\sim 4.5\text{nm}$  (LPC0, a large version of a PC0 device) and  $\sim 6\text{nm}$  (PC1) were used to measure  $\text{F K}\alpha$  X-rays. LDEs offer greater count rates, decreased spectral resolution (reducing peak shape and shift effects) and multiple-order X-ray suppression (in particular, suppressing the 3<sup>rd</sup>-order  $\text{P K}\alpha$  peak) in comparison to TAP or LTAP crystals. LPC0 was used on the SX-100 instrument, while PC1 was used on a CAMECA Camebax instrument.

As a check of the accuracy of the analytical protocol, seven synthetic apatites ranging from end-member fluorapatite to end-member chlorapatite, synthesized and analyzed by wet chemistry as described in Schettler et al. (2011), were mounted in epoxy in a **c**-axis normal to the electron beam orientation, polished and carbon-coated.

For studies on the effect of different metal coatings, the Wilberforce samples were repolished and coated either with aluminum by high vacuum evaporation of Al wire from a heated W-basket or with gold by magnetron sputter coating. The film thicknesses were calculated using GMRFILM software (Waldo 1988, 1991), based on measurements of Al and Au X-ray intensities measured from the coated samples.

For the initial cryostage experiments, two small wafers of the Wilberforce apatite specimen, each approximately 4 mm x 8 mm x 2 mm thick, were hand-polished, cemented to an aluminum stub with colloidal silver, and carbon-coated. One piece was mounted on its edge so that the **c**-axis was normal to the electron beam, while the other

sample was mounted flat so that the **c**-axis was parallel to the beam. The smaller sample size, as compared to a conventional epoxy plug, allowed for maximum thermal contact between the cold metal plate of the stage and the apatite. Further cryostage studies utilized apatite samples embedded in epoxy resin with their **c**-axes parallel to the electron beam set in 0.1875" holes drilled in a 1.0" diameter by 0.20" thick brass cylinder, which was subsequently polished and carbon-coated. The cold temperature work was performed with a Hexland CT-1000 cryostage mounted on a CAMECA Camebax MICROBEAM instrument running Macintosh automation software (Henderson, 1990). An in-chamber cold plate set to -190 C was used during the experiment to prevent contamination buildup on the surface of the apatite sample.

A separate study of similar apatite samples was carried out in this laboratory by Wang et al. (2011), whose purpose was to calibrate the IR technique for the accurate measurement of OH in apatite, with absolute concentrations obtained by the elastic recoil detection (ERD) method (e.g., Tirira et al. 1991; Aubaud et al. 2009; Bureau et al. 2009; Cherniak et al. 2010). ERD measurements of H concentrations were made on large polished and crack-free samples, whereas polarized FTIR measurements were made on oriented single apatite crystal wafers polished to  $\leq 60 \mu\text{m}$  thickness with the **E** vector parallel to the **c**-axis (Bhatnagar 1967; Levitt and Condrate Sr. 1970; Libowitzky et al. 1996). All of these measurements were made at the University of Michigan. Details can be found in Wang et al. (2011). The results were used for comparison with electron microprobe analyses obtained in this study.



## RESULTS

### Time scans

Time scans of approximately six minutes in duration were collected on oriented samples of the Durango, Wilberforce and High Atlas Mountain samples for F X-rays at a 15 kV accelerating voltage over an array of beam currents from 2 to 15 nA and spot sizes from a focused spot to 10  $\mu\text{m}$  in diameter. Larger spot sizes were not considered, due to concerns with WDS defocusing effects and loss of true “micro”-analysis capabilities. One hundred 3-s counting periods were acquired. Due to data transfer overhead, the actual beam exposure time was longer, and data are shown in terms of true beam exposure time. The beam was not blanked between counting periods. Longer total acquisition times were not deemed necessary, as the intent of the experiment was to determine beam conditions yielding stable or predictably-varying major element X-ray count rates to be measured at the beginning of an analytical sequence and with reasonable count times. Raw count rate data was converted, on a first-order basis, to a F weight percent value and plotted (Figures 1-6). Since the first data point was collected after a 3 s counting period, any rapid changes in count rate during the first few seconds are not resolvable.

The time scan results for the Durango apatite, which contains 3.53 wt% F, 0.41 wt% Cl, and 0.085 wt% H<sub>2</sub>O (Young et al. 1969; Wang et al. 2011), show the F X-ray count rate dependence on beam direction, current, and spot size (Figures 1 and 2). When the electron beam is parallel to **c**-axis (Figure 1) and when the beam current is 5-15 nA, the F count rate (and hence the calculated F concentration) decreases by almost 40% in the first 30 s for a focused beam, but increases by 5-10% for 2-10  $\mu\text{m}$  beam spots. For 5 and 10

$\mu\text{m}$  beam spot sizes, the count rate first increases with time, reaches a maximum, and then decreases with time. When the beam current is decreased to 2 nA, the variation in count rates is smaller, but still amounts to  $>5\%$ . At none of the beam currents or spot sizes, is the measured F concentration accurate. The behavior over longer times is even more complex: there may be a second rise in the count rate. It is believed this is due to severe sample damage, such that the beam moved off its initial location on the sample, due to loss of the conductive coating, and started exciting an adjacent region.

When the beam current is perpendicular to the **c**-axis (Figure 2), a focused beam still causes significant F count rate variation. However, when the beam spot size is 2-10  $\mu\text{m}$ , not only is the variation of F count rate small in the first 30 s, but also the measured F concentration is close to the actual concentration. However, at longer times, there may still be complicated behavior in the F count rate versus time. These observations (both Figures 1 and 2) are in agreement with the results of Stormer et al. (1993).

For the Wilberforce apatite, a near end-member fluorapatite containing between 3.4 (Webster et al. 2009) and 3.67 wt% F (analysis from the USGS, 1972) and no measurable Cl, results similar to those for Durango apatite were obtained, although in detail there are differences (Figures 3 and 4). For example, in the case with the **c**-axis parallel to the beam, F enrichment times were faster than seen in the Durango apatite. At all focused spot beam conditions, the F count rate started at its maximum and dropped; the enrichment was almost instantaneous (Figure 3). Severe sample damage was more evident at high beam current densities (Figure 3a) than on the Durango apatite. The analyses with the beam perpendicular to the **c**-axis show that a 2  $\mu\text{m}$  beam size is too

small when the beam current is 10-15 nA: a 5-10  $\mu\text{m}$  spot size is necessary to achieve good analyses.

The High Atlas Mountain (HAM) samples (Figures 5-6), an intermediate F-OH-Cl apatite containing 2.51 wt% F and 0.33 wt% Cl (as measured in this study), and 0.51 wt%  $\text{H}_2\text{O}$  (Wang et al. 2011), showed F count rate behavior similar to the Durango and Wilberforce apatite. The highest tested beam current density (e.g., 15 nA and small spot sizes) time scans on the **c**-axis parallel to the beam sample again showed only a decline from an zero time F count rate which corresponds to a greater than expected F concentration.

For all three apatite samples, when the electron beam is parallel to the crystallographic **c**-axis, the extrapolated F count rate to zero time corresponds to a concentration greater than the sample's nominal F concentration. Extrapolation can be made by eye from the time scan plots or by software linear regression of sub-counting periods during the first 30s or so of beam exposure. For samples oriented with the **c**-axis perpendicular to the beam, if the beam size is 5-10  $\mu\text{m}$ , the measured concentration is similar to the nominal concentration without extrapolation. However, if the beam size is smaller, extrapolation back to zero time is necessary and roughly yields an initial count rate consistent with each sample's nominal F concentration.

Cl time-dependence was evaluated on the synthetic chlorapatite synthesized by Prowatke. Unfortunately, oriented grains of this sample were not available. However, at all beam conditions, Cl count rates (Figure 7) were less volatile than F rates seen in the fluorapatite samples, as was also found by Stormer et al. (1993). Cl count rates using smaller beam sizes (focused and 2  $\mu\text{m}$ ) do show variations with time, similar to those

observed for F in the fluorapatites, but 5-10  $\mu\text{m}$  beam sizes yield stable Cl count rates. No statistically significant variation was seen in the Cl count rates between several randomly-oriented grains when measured with a 15 kV, 10 nA and 10  $\mu\text{m}$  diameter beam, confirming a minimal orientation effect at these beam conditions.

After assessing the time scans on these four apatite samples, a 15 kV, 10 nA, and 10  $\mu\text{m}$  diameter beam condition was chosen for subsequent quantitative analysis work. For Cl-rich apatite compositions, a smaller beam size and/or higher beam current might yield acceptable count rate stability, but the chosen conditions showed constant or predictably varying F and Cl count rates during the time period needed for major element analysis of all apatite compositions evaluated in this study.

### **Selection of F standards and spectral measurement settings**

Wavelength spectra were acquired for F  $K\alpha$  X-rays from fluorite, fluortopaz,  $\text{MgF}_2$  and the Wilberforce fluorapatite (Figure 8). There was little apparent peak shape change or peak position shift seen between these four materials, when using the LPC0 LDE (d-spacing of  $\sim 4.5$  nm) or PC1 LDE (d-spacing of  $\sim 6$  nm). Narrow background offset positions for F (-1250 and +1000 steps for LPC0, compared to a more conventional  $\pm 3000$  steps, and  $\pm 600$  steps for PC1, compared to  $\pm 2300$  steps) were chosen to avoid the nearby 2<sup>nd</sup> order Mg and Al peaks noted by Raudsepp (1995). This is especially important given that the potential F standards  $\text{MgF}_2$  and fluortopaz contain high concentrations of Mg and Al. Even though the chosen background positions are on the shoulders of the F  $K\alpha$  peak, the specimen to standard intensity ratio is not affected (Reed 1993). While a Fe  $L\alpha$  X-ray overlap on the shoulder of the F  $K\alpha$  peak (Potts and Tindle

1989) is a potential problem for accurate F analysis and Witter and Kuehner (2004) offer a solution, there is very little Fe in the apatites studied here and the overlap was ignored.

Time scans of F X-rays were taken on fluorite, fluortopaz, and  $MgF_2$ . The  $MgF_2$  and fluortopaz F intensities were stable for the duration of the scan, while the intensity from fluorite dropped immediately, approaching 85% of its original intensity after 5 minutes of beam exposure (Figure 9). At higher beam current densities, fluorite is quickly and visibly damaged. Its use as a fluorine standard is therefore not recommended for these beam conditions and its use was dropped from further analytical consideration.

### **X-ray mapping**

Before selection of analysis locations, backscattered electron (BSE) images and X-ray maps for several elements (Na, S, Ce, F or Si and Cl) were acquired on the oriented apatite samples to check for chemical homogeneity. Though a lengthy process, X-ray mapping revealed chemical zoning in several apatites that was not readily apparent in the BSE images. The Wilberforce, Durango, Gem3 and Silver Crater Mine apatites (Figures 10-14) showed various degrees of zoning in Na, S, and Ce. F and Cl zoning was not apparent in most X-ray maps, possibly due to their higher concentrations (and correspondingly smaller relative variations) compared to the other mapped minor elements. The Asparagus Stone (Durango) sample did show Cl zoning (Figure 12b), which was verified by subsequent analysis to range between 0.42 and 0.55 wt.% Cl. Boyce and Hodges (2005) identified Th and Si variation in the Durango apatite by X-ray mapping at high beam currents. The Silver Crater Mine sample showed the most chemical variation, with numerous inclusions and patchy textures, while the High Atlas

Mountains sample showed virtually no chemical zoning (Figure 15). The Asparagus Stone sample of Durango apatite was also imaged by cathodoluminescence (CL) (Figure 16). The CL image reveals small variations in signal corresponding to changes in elemental concentrations as seen by X-ray mapping and appears to be a more sensitive technique than BSE imaging for quickly finding sample heterogeneities.

Because X-ray mapping and long-duration CL imaging expose the surface of the apatite grains to a high electron flux, the samples were repolished and carbon-coated before continuing with quantitative analysis. The critical light-element standards of fluorapatite,  $\text{MgF}_2$  and chlorapatite were carbon-coated in the same run as the oriented apatite samples.

### **Quantitative analysis**

Given the large number of possible elemental substitutions in apatite (Pan and Fleet 2002), a 28-element analytical package was assembled for use as a general-purpose apatite routine. Following the recommendations of Pyle et al. (2002), the major elements Ca, P, O, F and Cl were analyzed at the beginning of the sequence, using a 15 kV, 10 nA and 10  $\mu\text{m}$  diameter beam. F and Cl were measured with five sub-counting periods of 6 s duration, which were linearly regressed to give a zero time count rate (after Nielsen and Sigurdsson 1981). Additional elements were analyzed at this first beam condition before a second, higher beam energy and current condition of 20 kV, 20 nA and 10  $\mu\text{m}$  beam diameter was used to analyze a second set of elements, including the REE, which were expected to be present in small concentrations or whose X-ray lines were more efficiently excited by a 20 kV beam.

F was calibrated on both MgF<sub>2</sub> and fluortopaz to check for a difference in analytical results obtained using these two standards. Synthetic chlorapatite was used as the calibration standard for the major elements of Ca, P, Cl and O, while various other natural and synthetic materials were used as standards for minor and trace elements. The complete setup of analyzed elements, X-ray lines, analyzing crystals, background offsets, PHA modes and calibration standards is listed in the Appendix.

Tables 1 and 2 summarize the results for the apatite samples oriented with the crystallographic *c*-axis perpendicular to the beam. In the results presented here, O was calculated by stoichiometry, but direct O analyses are also listed for comparison. F values from the *c*-axis parallel to the beam samples (Table 3) were higher than the *c*-axis perpendicular to the beam samples by 1-15% relative, even when using the zero time sub-counting routine during analysis. This discrepancy is to be expected after noting elevated zero time intercepts for F on the time scans used for beam condition selection (Figures 1, 3 and 5). There was no statistically significant difference in the measured concentrations of the other major elements, P, Ca, Cl, and O, between the two sample orientations, at these beam conditions and with these counting times.

The analytical data are in good agreement with literature chemical analyses for the Durango and Wilberforce apatites (Table 4). Because of chemical zoning, as seen by X-ray mapping, there will be slight differences between the EPMA measured values in this study and those values from bulk analysis in the literature. It would not be practical to accurately integrate the chemical zoning at the microscopic level in order to present a representative bulk analysis for a given apatite locality, due to variability in collected samples and their mounted sections.

F analyses calibrated against the fluortopaz standard were ~5% relative higher than those analyses calibrated against MgF<sub>2</sub>. Solberg (1982) noted similar problems when analyzing a fluortopaz against other F standards and demonstrated a marked peak shape and position shift between topaz and several other F-bearing materials. Solberg used a RAP crystal, which has much higher spectral resolution (and much lower intensities) than the LDEs used in this study. Area peak factor (APF) calculations (Bastin and Heilijgers 1991) from wavelength spectra acquired from the LPC0 LDE used in this study yielded a value of 1.003 for fluortopaz relative to MgF<sub>2</sub>, showing a minimal F K $\alpha$  peak shape change between these two standards. The F K $\alpha$  peak position shift between MgF<sub>2</sub> and fluortopaz was also very slight, approximately 10 steps on the spectrometer scale (each step represents 0.00001 sin  $\theta$ ), and was not large enough to cause a significant intensity variation, given the relatively broad F K $\alpha$  peak. X-ray spectral effects, such as PHA distribution shifts between low and high count rates and F X-ray polarization controlled by sample crystallographic orientation in relation to the analyzing wavelength dispersive spectrometer, were checked, but not significant. The difference between results obtained with MgF<sub>2</sub> and fluortopaz was observed on two instruments and with different analyzing LDEs. Chemical analyses of 0.19 wt.% H<sub>2</sub>O (Penfield and Minor 1894) and 0.04 wt.% H<sub>2</sub>O (Barton et al. 1982) of the Topaz Mountain (Utah) topaz indicate that it is nearly pure F end-member. However a slightly higher OH content (5% of the OH-F site or 0.49 wt. % H<sub>2</sub>O), though unlikely, would be sufficient to bring the fluortopaz F intensity in line with the intensity measured from MgF<sub>2</sub>.

Normalization of the apatite analyses to five M-site cations in the general apatite formula of M<sub>5</sub>(Z<sub>4</sub>O<sub>4</sub>)<sub>3</sub>X yielded good sums for the cations assumed to be in the Z-site



(Table 2). IR spectroscopy and ERD results for H<sub>2</sub>O contents (Wang et al. 2011) correlate well with the calculated H<sub>2</sub>O from EMPA (Table 1). For the Silver Crater apatite, the F concentration by EMPA is in excess of 1 apfu, while there is also a deficit in the Z-site of 0.05 cpfu. IR spectroscopy shows CO<sub>3</sub><sup>2-</sup> bands in this sample, which supports the possibility of a coupled CO<sub>3</sub><sup>2-</sup> and F<sup>-</sup> substitution for PO<sub>4</sub><sup>3-</sup>, though Regnier et al. (1994) found no evidence for a specific CO<sub>3</sub>F<sup>3-</sup> group in apatites. The calculated CO<sub>2</sub> value listed in Table 1, assumes this coupled substitution.

A suite of synthetic apatite samples, ranging from fluorapatite to chlorapatite, was graciously provided by D. Harlov (personal communication) and mounted in an orientation with the c-axis perpendicular to the electron beam. The chemical compositions of these samples, described in Schettler et al. (2011), provide an additional reference for evaluating the EMPA apatite analytical procedure. Since the samples are synthetic, only the major elements (F, O, P, Ca and Cl) were analyzed by EMPA. The results are in excellent agreement with the wet chemical data (Table 5). Since the F results obtained with MgF<sub>2</sub> as the F standard were in good agreement with published wet chemical data for the Wilberforce and Durango apatites (Table 4) and the synthetic apatites of Schettler et al. (2011), it was decided to use MgF<sub>2</sub> as the F standard for the other apatites. Webster et al. (2009) also noted that their apatite analyses were more accurate when using MgF<sub>2</sub> or boracite than using other F standards (they did not mention which standards had been evaluated).

### **Alternative metal coatings**

The Wilberforce apatite sample showed the highest degree of F count rate orientation-controlled anisotropy, so it was selected as a test sample for evaluation of several

alternative analytical methods. Gold and aluminum have been used to coat minerals used in EMPA geochronology (Jercinovic and Williams 2005; Hetherington 2008), in order to increase electrical and thermal conductivity at the high beam currents required for trace element analysis of Pb, U and Th. In separate experiments, oriented samples of the Wilberforce apatite were coated with 40 nm of Au and Al. Plots of F count rate versus beam exposure time show similar profiles to scans acquired from carbon-coated samples (Figures 17 and 18). With the metal coatings, there was a change in behavior of the F temporal count rate compared to that from carbon-coated samples: instead of an initial decrease from a rate corresponding to a higher than expected count rate (see Figure 3a for the carbon coated sample measured at comparable conditions), the F count slowly increased to a maximum over the 360 s period of the time scan. However, samples oriented with the *c*-axis parallel to the beam still displayed zero time count rates higher than samples with the *c*-axis perpendicular to the beam. Trial quantitative analyses on both the Au- and Al-coated apatites, even with a zero time correction, showed a discrepancy in F concentrations between both orientations. For accurate F weight percent calculations, an absorption correction should be made for the presence of a Au or Al film. However, this was not attempted here once it was determined that neither the Au nor Al film eliminated the orientation effect for F.

### **Cryogenic cooling**

Time scans on two oriented chips of Wilberforce apatite were taken under beam conditions of 15 kV and 10 nA with a 10  $\mu\text{m}$  x 10  $\mu\text{m}$  rastered beam and are shown in Figure 19. A rastered beam was used due to hardware limitations on the older Camebax

instrument, where use of defocused spot beams is inconvenient and less reproducible in size than selection of a rastered beam. In theory there should be little difference in F count rate temporal variation when equivalently sized rastered and spot beams are used, though this was not explicitly tested in this study. Curve fits of the data show that the zero time count rate for the sample oriented with its **c**-axis parallel to the beam does not equal the rate for the **c**-axis perpendicular sample at room temperature. However, once the sample is cooled to lower temperatures, the discrepancy in zero time count rates between the two sample orientations disappears. Below -100 C, there is significant sample "icing", where the surface of the sample accumulates a contamination layer which interferes with the analysis of light elements, such as O and F. Figure 20 shows measured F concentrations for both sample orientations as a function of sample temperature. While the measured F concentration of the sample with the **c**-axis perpendicular to the beam does not change with temperature, the F concentration in the sample with **c**-axis parallel orientation does decrease with temperature and converges to the same value as the **c**-axis perpendicular sample at low temperatures.

Analytical results for mounted and polished oriented apatite samples are shown in Table 6 for a range of different beam sizes at cryogenic and room temperatures. The samples were oriented with the **c**-axis parallel to the beam. For the same beam size, the F results from cryogenically-cooled samples were lower than those measured at room temperature and approach the F compositions measured on **c**-axis perpendicular samples. Cryogenic cooling still does not allow accurate analysis with a focused spot beam, though it does appear to eliminate the discrepancy in measured F concentrations between the two sample orientations when a broader beam size is used.

### **Sample movement during analysis**

Lastly, the technique of moving the sample under the beam during analysis was evaluated (Webster et al. 2009). Stage movement during analysis can be automated, but the technique generally requires the presence of an alert EMPA operator during analysis to avoid moving the beam off the apatite sample or onto inclusions, surface pits or other flaws.

F compositions measured from three fluorapatite samples mounted in both **c**-axis parallel and **c**-axis perpendicular orientations and with static and moving samples are shown in Table 7 and Figure 21. As expected, results for moving and static analyses on the **c**-axis normal to the beam orientations are in good agreement with the nominal F values for all samples. When the **c**-axis is parallel to beam, F concentration is overestimated when the sample is static, but close to the true value when the sample is moved at a velocity of 4  $\mu\text{m/s}$  during analysis. Increasing the velocity further improves the accuracy. On the other hand, the Silver Crater Mine sample oriented with the beam parallel to the **c**-axis yields a slightly lower F value when using sample movement than the sample oriented with the **c**-axis perpendicular to the beam. This may be due to sample heterogeneity, which is seen in the X-ray and BSE images (Figure 14). The main disadvantage of this technique is the loss of small area analysis; however for large and homogeneous samples, sample movement during analysis appears to eliminate crystallographic orientation effects in F measurements.

## **DISCUSSION**

### **Comparison with previous studies**

As summarized in the Introduction, five studies (Stormer et al. 1993; Pyle et al. 2002; Webster et al. 2009; Adams et al. 2010; and McCubbin et al. 2010) documented various conditions to analyze apatite by electron microprobe, with special focus on F due to its mobility under electron beam bombardment. The results in this study are in general agreement with the studies of Stormer et al. (1993). On the other hand, the suggestion by Pyle et al. (2002) to analyze F with short counting times at the beginning of an analytical sequence is not sufficient to obtain accurate concentrations; for example, Figures 1 and 3 show that even at short counting times (e.g., 3 s), the apparent concentration based on the count rate can still be significantly different from the known concentration if the beam is parallel to **c**.

The results of this study support the analytical approach used by Webster et al. (2009), namely the use of sample movement with a moderate beam current (10 nA) and defocused beam (6-20  $\mu\text{m}$  diameter), with  $\text{MgF}_2$  used as the F calibration standard. Adams et al. (2010) showed TDI curves acquired over very long times of nearly one hour, an impractical time for routine microanalysis. The details during the first few minutes of acquisition of their TDI curves were similar to those seen from Durango apatite in this study and showed the same zero time discrepancy between **c**-axis parallel and **c**-axis perpendicular orientations. McCubbin et al. (2010) used TDI curves as a test for post-analysis acceptance, discarding analyses with curves showing negative or non-linear slopes. Though they could not correlate crystallographic orientation with the trends in their TDI data, it seems likely they were observing the same orientation effects

seen here. Negatively-sloped TDI curves seen in this study always yielded higher-than-expected zero time F intercepts and concentrations. Thus, their analyses with negatively-sloped TDI curves were correctly rejected. Their choice to use positively-sloping, linear TDI data as a criterion for analysis acceptance is less clearly supported by the results of this study, however.

### **Recommended protocol for electron microprobe analyses of apatite**

Accurate electron beam microanalysis of apatite is a non-trivial exercise, given the mineral's demonstrated beam sensitivity and crystallographic orientation effects. Techniques used to analyze other beam-sensitive materials were applied to analysis of apatite in the study, with mixed success, and the following recommendations can be made, many of which echo those of Stormer et al. (1993), Webster et al. (2009) and McCubbin et al. (2010):

- 1) If at all possible, avoid analyzing apatite grains oriented with the **c**-axis parallel to the electron beam, especially for fluorapatite. Even with a zero time correction, F count rates from this orientation will be extrapolated to a value that is systematically too high. Values from apatites of unknown orientation should be regarded as representing an upper limit of true F concentration. As apatite F concentration decreases, the orientation-related discrepancy in F also decreases.

- 2) Avoid the use of high beam currents and finely-focused, or spot, beams. A beam current of 15 nA or less and a beam diameter of 5  $\mu\text{m}$  or larger are recommended. If it is feasible to move the sample under the beam during

analysis, the results are more likely to be accurate. Cryogenic cooling of the sample during analysis slows the rate of change of the F count rate and allows the use of smaller spot sizes on all sample orientations. However, the use of a cryogenic stage can be cumbersome and is not an available option in most labs.

3) Given that F and, to a lesser extent, Cl count rates vary with time under almost all typically-used beam conditions, a zero time correction counting routine should be used to measure those elements. If possible, time scans should be performed prior to analysis to validate the choice of electron beam conditions on the particular instrument used for analysis. Rejection of analyses based on negatively-sloped TDI curves (McCubbin et al. 2010) is confirmed by detailed TDI curves seen from oriented apatites in this study. However, positively-sloped TDI curves do not ensure a zero time F value corresponding to the true F concentration.

4) F-rich apatites, including the Durango and Wilberforce fluorapatites, are not recommended as primary microanalysis standards. As Stormer et al. (1993) showed, once an area has been damaged by electron beam exposure, its composition is permanently changed, so relying on these materials to remain in an unblemished condition, especially in a multi-user laboratory, is optimistic. Aside from concerns with crystallographic orientation effects, there is also evidence of elemental zoning in the Durango and Wilberforce samples. Synthetic  $\text{MgF}_2$  appears to be a good F standard for apatites, while a Cl-rich apatite is a more robust choice than a fluorapatite standard for Ca, P and O calibration.

In summary, three approaches to electron microprobe analysis of apatites seem to be able to produce accurate F concentration:

(1) If the apatite sample can be oriented, prepare apatite grains so that the electron beam is perpendicular to **c**-axis. Use a defocused or rastered beam of  $\geq 5 \mu\text{m}$  diameter and a beam current of  $\leq 10 \text{ nA}$ .

(2) For large apatite crystals without fractures, inclusions or polishing pits, use a sample movement technique with a velocity of  $\geq 4 \mu\text{m/s}$  and a defocused or rastered beam of  $\geq 5 \mu\text{m}$  diameter and a beam current of  $\leq 10 \text{ nA}$ .

(3) If a cryogenic system is available, cool the sample to about  $-80^\circ\text{C}$ , and use a rastered or defocused beam of  $\geq 5 \mu\text{m}$  diameter and a beam current  $\leq 10 \text{ nA}$ , with software extrapolation to a zero time counting rate.



## **Acknowledgements**

It would not have been possible to complete this study without the help of many individuals. I would like to thank Youxue Zhang and Karen Wang for procurement and sectioning of the oriented natural apatite samples, Dan Harlov for providing synthetic apatite samples and Zach Sharp for providing the synthetic chlorapatite material. The manuscript benefitted greatly from comments by Youxue Zhang and Rod Ewing. This study is dedicated to the memory of Eric J. Essene, who mentored me for many years and inspired this study, and to the many friends and family who have encouraged and supported me over the past several years, especially Carol, Jim, Anja, Rachel, Peter, Shirley and Pete. This research is partially supported by NSF Grant EAR-0838127, while the electron microprobes used in this study were partially funded by NSF Grants EAR-8212764 and EAR-9911352.

## **References Cited**

- Adams, D.T., Koenig, A.E., and Lowers, H.A. (2010) Apatite revisited: the role of anisotropy in apatite analysis. *Microscopy and Microanalysis* 16, Suppl. 2.
- Aubaud, C., Bureau, H., Raepsaet, C., Khodja, H., Withers, A.C., Hirschmann, M.M., and Bell, D.R. (2009) Calibration of the infrared molar absorption coefficients for H in olivine, clinopyroxene and rhyolitic glass by elastic recoil detection analysis. *Chemical Geology*, 262, 78-86.

Barton, M.D., Haselton, H.T., Hemingway, B.S., Kleppa, O.J. and Robie, R.A. (1982) The thermodynamic properties of fluor-topaz. *American Mineralogist*, 67, 350-355.

Bastin, G.F. and Heijligers, H.J.M. (1991) Quantitative Electron Probe Microanalysis of Ultra-Light Elements (Boron-Oxygen), in *Electron Probe Quantitation (K.F.J. Heinrich and D.E. Newbury, eds.)*, Plenum Press, New York, 145-175.

Bhatnagar, V.M. (1967) Infrared spectrum of an apatite from Wilberforce, Ontario, Canada. *Archives of Oral Biology*, 12, 429-430.

Boyce, J.W. & Hodges, K.V. (2005) U and Th zoning in Cerro de Mercado (Durango, Mexico) fluorapatite: insights regarding the impact of recoil redistribution of radiogenic  $^4\text{He}$  on (U-Th)/He thermochronology. *Chemical Geology*, 219, 261-274.

Bureau, H., Raepsaet, C., Khodja, H., Carraro, A., and Aubaud, C. (2009) Determination of hydrogen content in geological samples using elastic recoil detection analysis (ERDA). *Geochimica Cosmochimica Acta*, 73, 3311-3322.

Cherniak, D.J., Hervig, R.L., Koepke, J., Zhang, Y., and Zhao, D. (2010) Analytical methods in diffusion studies. *Reviews of Mineralogy and Geochemistry*, 72, 107-170.

Devine, J.D., Gardner, J.E., Brack, H.P, Layne, G.D., Rutherford, M.J. (1995) Comparison of analytical techniques for estimating  $\text{H}_2\text{O}$  contents of silicic volcanic glasses. *American Mineralogist*, 80, 319-328.

Henderson, C.E. (1990) A Macintosh interface for the CAMECA Camebax-MICROBEAM electron microprobe. Proceedings of the XIIth International Congress for Electron Microscope, Vol. 1, 438-439.

Hetherington, C.J., Jercinovic, M.J., Williams, M.L. and Mahan, K. (2008) Understanding geologic processes with xenotime: Composition, chronology, and a protocol for electron probe microanalysis. *Chemical Geology*, 254, 133-147.

Jercinovic, M.J. and Williams, M.L. (2005) Analytical perils (and progress) in electron microprobe trace element analysis applied to geochronology: Background acquisition, interferences, and beam irradiation effects. *American Mineralogist*, 90, 526-546.

Kearns, S.L., Steen, N. and Erlund, E. (2002) Electronprobe microanalysis of volcanic glass at cryogenic temperatures. *Microscopy and Microanalysis*, 8, Suppl. 2, 1562CD.

Kerrick, D.M., Eminhizer, L.B. & Villaume, J.F. (1973) The role of carbon film thickness in electron microprobe analysis. *American Mineralogist*, 58, 920-925.

Levitt, S.R., and Condrate Sr., R.A. (1970) The polarized infrared spectra of hydroxyl ion in fluorapatite. *Applied Spectroscopy*, 24, 288-289.

Libowitzky, E., and Rossman, G.R. (1996) Principles of quantitative absorbance measurements in anisotropic crystals. *Physics and Chemistry of Minerals*, 23, 319-327.

McCubbin, F.M., Steele, A., Nekvasil, H., Schnieders, A., Rose, T., Fries, M., Carpenter, P.K., and Jolliff, B.L. (2010) Detection of structurally bound hydroxyl in fluorapatite from Apollo Mare basalt 15058,128 using TOF-SIMS, *American Mineralogist*, 95, 1141-1150.

Morgan, G.B., VI, and London, D. (1996) Optimizing the electron microprobe analysis of hydrous alkali aluminosilicate glasses. *American Mineralogist*, 81, 1176-1185.

Morgan, G.B., VI, and London, D. (2005) Effect of current density on the electron microprobe analysis of alkali aluminosilicate glasses. *American Mineralogist*, 90, 1131-1138.

Nielsen, C.H. and Sigurdsson, H. (1980) Cryogenic elimination of sodium loss in glasses during EPMA analysis. *Microbeam Analysis*, 139-142.

Nielsen, C.H. and Sigurdsson, H. (1981) Quantitative methods for electron microprobe analysis of sodium in natural and synthetic glasses. *American Mineralogist*, 66, 547-552.

Pan, Y. & Fleet, M.E. (2002) Compositions of the Apatite-Group Minerals: Substitution Mechanisms and Controlling Factors. *Rev. Mineral. Geochem.* 48, 13-49.

Penfield, S.L. and Minor, Jr., J.C. (1894) On the chemical composition and related physical properties of topaz. *American Journal of Science*, 3<sup>rd</sup> Series, 47, 387-396.

Potts, P.J. and Tindle, A.G. (1989) Analytical characteristics of a multilayer dispersion element ( $2d = 60 \text{ \AA}$ ) in the determination of fluorine in minerals by electron microprobe. *Mineralogical Magazine*, 53, 357-362.

Pyle, J.M., Spear, F.M. & Wark D.A. (2002) Electron Microprobe Analysis of REE in Apatite, Monazite and Xenotime: Protocols and Pitfalls. *Rev. Mineral. Geochem.* 48, 337-362.

Raudsepp, M. (1995) Recent advances in the electron-probe micro-analysis of minerals for the light elements. *The Canadian Mineralogist*, 33, 203-218.

Reed, S.J.B. (1993) *Electron Microprobe Analysis*, 2<sup>nd</sup> ed., Cambridge University Press.

Regnier, P., Lasaga, A.C., Berner, R.A., Han, O.H. and Zilm, K.W. (1994) Mechanism of  $\text{CO}_3^{2-}$  substitution in carbonate-fluorapatite: evidence from FTIR spectroscopy,  $^{13}\text{C}$  NMR and quantum mechanical calculations. *American Mineralogist*, 79, 809-818.

Schettler, G., Gottschalk, M., and Harlov, D.E. (2011) A new semi-micro wet chemical method for apatite analysis and its application to the crystal chemistry of fluorapatite-chlorapatite solid solutions. *American Mineralogist*, 96, 138-152.

Smith, M.P. (1986) Silver coating inhibits electron microprobe beam damage of carbonates. *Journal of Sedimentary Petrology*, 56, no. 4, 560-561.

Solberg, T. N. (1982) Fluorine electron microprobe analysis: variations of X-ray peak shape. *Microbeam Analysis*, 148-150.

Stormer, J.C. Jr., Pierson, M.L. & Tacker, R.C. (1993) Variation of F and Cl X-ray intensity due to anisotropic diffusion in apatite during electron microprobe analysis. *American Mineralogist*, 78, 641-648.

Stormer, J.C. Jr. & Pierson, M.L. (1993) Variation of F and Cl X-ray intensity due to anisotropic diffusion in apatite during electron microprobe analysis: An addendum.

[http://www.minsocam.org/MSA/AmMin/Supplemental\\_Data/Stormer.html](http://www.minsocam.org/MSA/AmMin/Supplemental_Data/Stormer.html)

Tirira, J., Frontier, J.P., Trocellier, P., and Trouslard, P. (1991) Development of a simulation algorithm for energy spectra of elastic recoil spectrometry. *Nuclear Instruments and Methods in Physics Research B*, 54, 328-333.

Waldo, R.A. (1988) An iteration procedure to calculate film compositions and thicknesses in electron-probe microanalysis. *Microbeam Analysis*, 310-314.

Waldo, R.A. (1991) A characteristic fluorescence correction for thin-film analysis by electron microprobe. *Microbeam Analysis*, 45-53.

Wang, K.L., Zhang, Y., and Naab, F.U. (2011) Calibration for IR measurements of OH in apatite. *American Mineralogist*, revised.

Webster, J.D., Tappen, C.M. and Mandeville, C.W. (2009) Partitioning behavior of chlorine and fluorine in the system apatite-melt-liquid. II: Felsic silicate systems at 200 MPa. *Geochimica et Cosmochimica Acta* 73, 559-581.

Witter, J.B. & Kuehner, S.M. (2004) A simple empirical method for high-quality electron microprobe analysis of fluorine at trace levels in Fe-bearing minerals and glasses. *American Mineralogist*, 89, 57-63.

Young, E.J., Myers, A.T., Munson, E.L & Conklin, N.M. (1969) Mineralogy and geochemistry of fluorapatite from Cerro de Mercado, Durango, Mexico. USGS Professional Paper 650-D, D84-D93.

## APPENDIX

### ANALYTICAL SETUP FOR QUANTITATIVE ANALYSIS OF APATITE

Beam condition 1: 15 kV, 10 nA, 10  $\mu$ m spot size  
Background offsets are in  $\sin \theta \times 10^5$  units.

Element	X-ray Line	Spectro. and Device	Peak counting time	Standard	PHA mode	Background Offset 1	Background Offset 2
F*	<i>Ka</i>	1 LPC0	30	MGF2	Integral	-1250	1000
Na	<i>Ka</i>	1 LPC0	30	JADE	Integral	-2200	2500
O	<i>Ka</i>	1 LPC0	20	CACL AP	Integral	-2500	3900
Ca	<i>Ka</i>	2 PET	20	CACL AP	Integral	-700	1300
Cl*	<i>Ka</i>	2 PET	30	CACL AP	Integral	-600	600
K	<i>Ka</i>	2 PET	20	GKFS	Integral	-530	1100
S	<i>Ka</i>	2 PET	20	ANHY	Integral	-1300	1500
Fe	<i>Ka</i>	3 LLIF	40	FESI	Integral	-1200	1250
Mn	<i>Ka</i>	3 LLIF	40	BHRH	Integral	-1200	1600
Ba	<i>Ka</i>	4 LLIF	40	SANB	Integral	-1400	900
V	<i>Ka</i>	4 LLIF	40	V2O5	Integral	-700	700
Al	<i>Ka</i>	5 TAP	20	FTOP	Integral	-850	850
P	<i>Ka</i>	5 TAP	20	CACL AP	Diff. Auto	-500	400
Si	<i>Ka</i>	5 TAP	20	FTOP	Integral	-760	800
Mg	<i>Ka</i>	5 TAP	20	MGSI	Integral	-1600	1000

- F and Cl analyzed are the first elements analyzed on their respective spectrometers and are measured with a sub-counting routine consisting of five 6 s count periods, linearly extrapolated to a zero time count rate.

Beam condition 2: 20 kV, 20 nA, 10  $\mu$ m spot size

Element	X-ray Line	Spectro. and Device	Peak counting time	Standard	PHA mode	Background Offset 1	Background Offset 2	Background Slope
Pb	<i>Ma</i>	2 PET	30	ALAM	Integral	-1800	600	
Th	<i>Ma</i>	2 PET	25	THSIO4	Integral	-1300	800	
U	<i>Mb</i>	2 PET	25	UO2	Integral	-1250		0.95
As	<i>La</i>	5 TAP	20	ASP	Integral	-700	900	
La	<i>La</i>	3 LLIF	20	LAPO4	Integral	-670	810	
Ce	<i>La</i>	3 LLIF	20	CEPO4	Integral	-700	700	
Pr	<i>Lb</i>	3 LLIF	20	PRPO4	Integral	-450	450	
Nd	<i>La</i>	4 LLIF	20	NDPO4	Integral	-915	605	
Sm	<i>Lb</i>	4 LLIF	20	SMPO4	Integral	-500	570	
Gd	<i>Lb</i>	4 LLIF	20	GDPO4	Integral	-440	530	
Dy	<i>La</i>	4 LLIF	20	DYPO4	Integral	-260	450	
Sr	<i>La</i>	5 TAP	40	SRTIO3	Diff. Auto		450	0.90
Y	<i>La</i>	5 TAP	40	YAG	Integral	-300	300	



Standards:

MGF2	MgF <sub>2</sub> , synthetic
FTOP	Fluortopaz, natural
JADE	Jadeite, JD-1, natural
CACL AP	Ca-Cl apatite, synthetic
GKFS	Adularia, St. Gothard, natural
ANHY	Anhydrite, natural
FESI	Ferrosilite, synthetic
BHRH	Rhodonite, Broken Hill
SANB	Sanbornite, natural
V2O5	V <sub>2</sub> O <sub>5</sub> , synthetic
MGSI	MgSiO <sub>3</sub> glass, synthetic
ALAM	Alamosite, natural
ASP	Arsenopyrite, natural
YAG	Yttrium aluminum garnet, synthetic
UO2	Uraninite, syn
LAPO4	LaPO <sub>4</sub> , synthetic
CEPO4	CePO <sub>4</sub> , synthetic
PRPO4	PrPO <sub>4</sub> , synthetic
NDPO4	NdPO <sub>4</sub> , synthetic
SMPO4	SmPO <sub>4</sub> , synthetic
GDPO4	GdPO <sub>4</sub> , synthetic
DYPO4	DyPO <sub>4</sub> , synthetic
SRTIO3	SrTiO <sub>3</sub> , synthetic

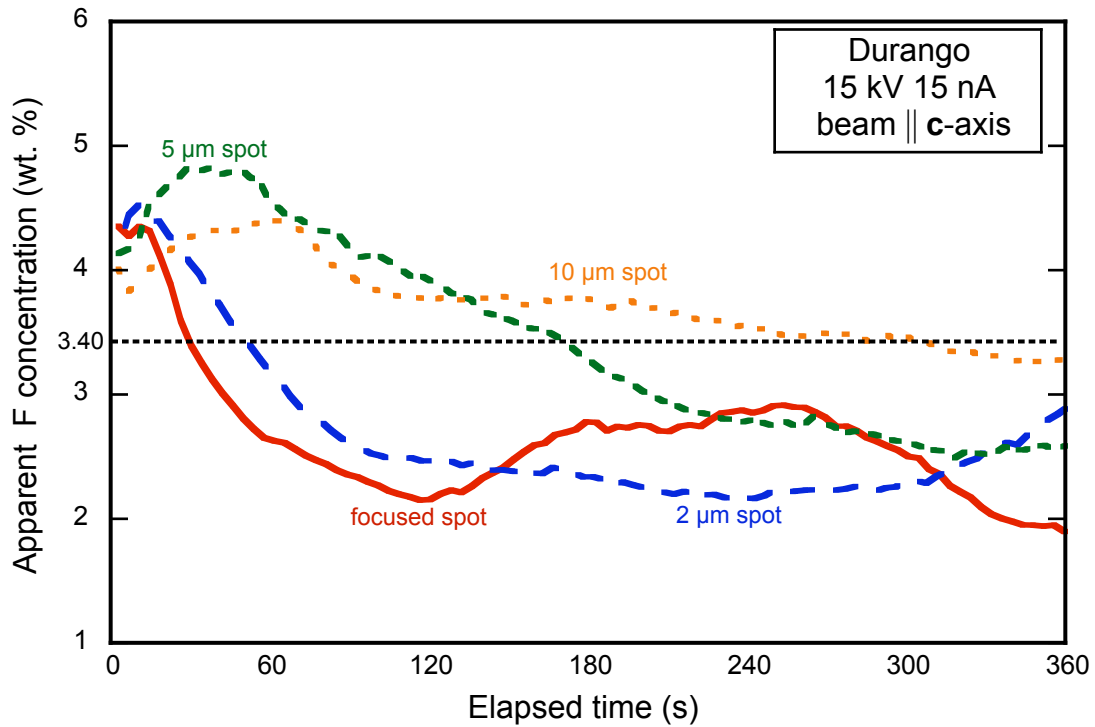


**Figure 1a.** Apparent F concentration with time for different beam spot sizes measured on Durango apatite oriented with the c-axis parallel to the beam at 15 kV and 15 nA.

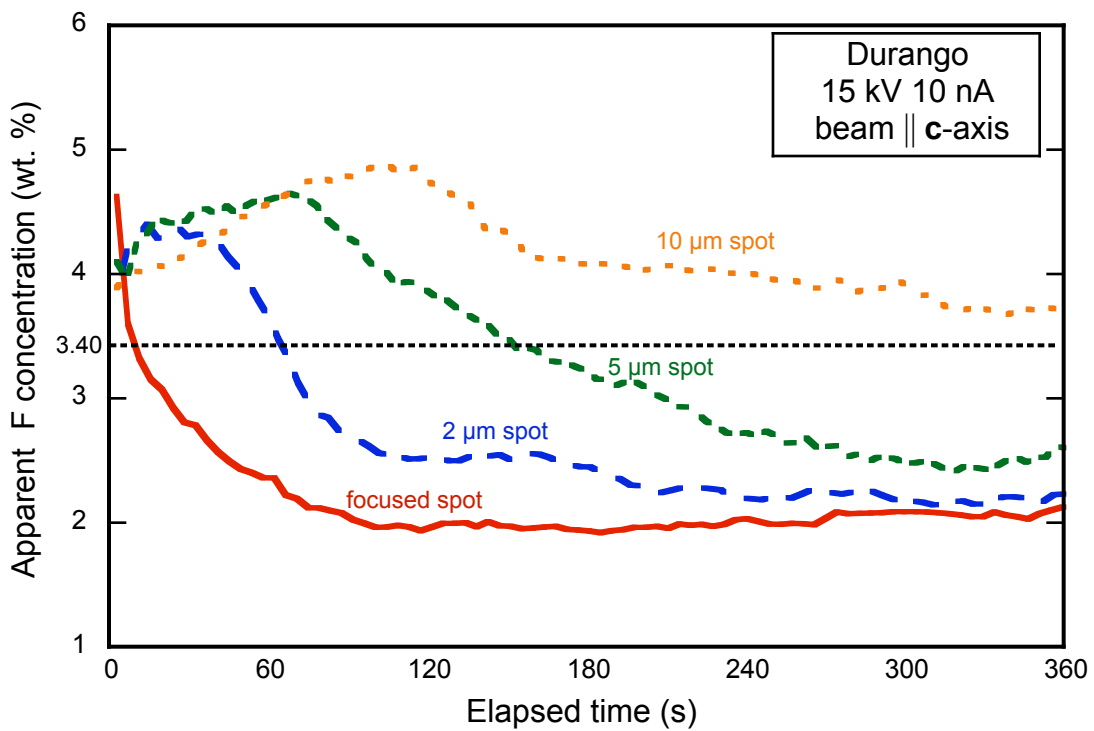


**Figure 1b.** Apparent F concentration with time for different beam spot sizes measured on Durango apatite oriented with the c-axis parallel to the beam at 15 kV and 10 nA.

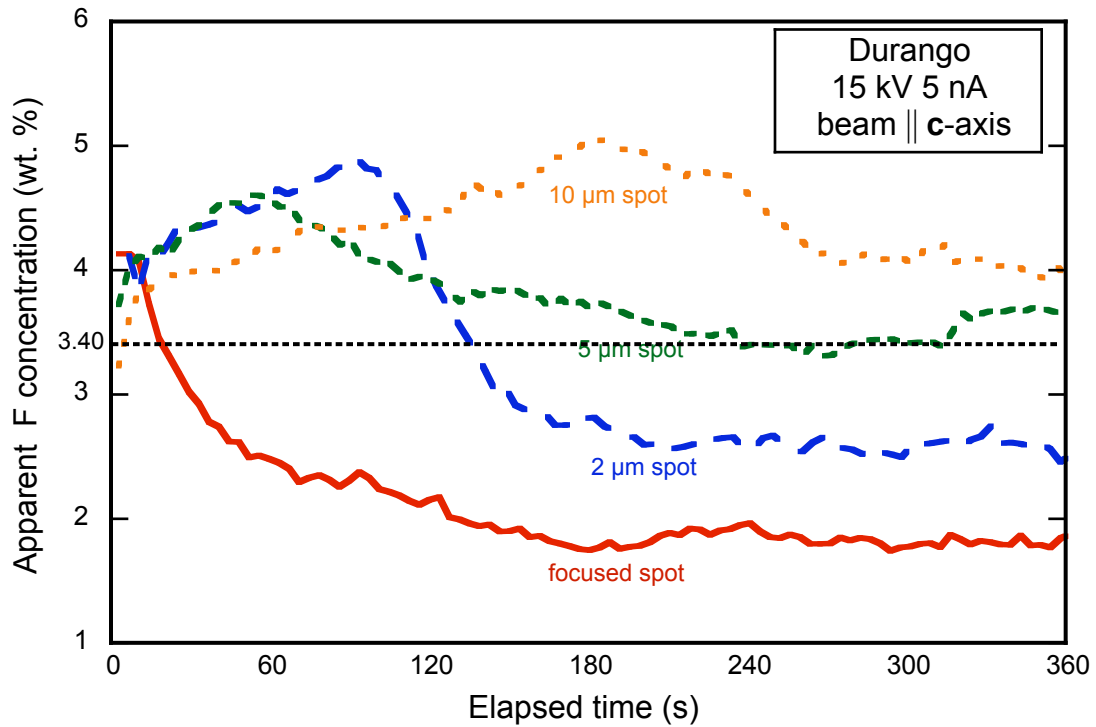


**Figure 1c.** Apparent F concentration with time for different beam spot sizes measured on Durango apatite oriented with the c-axis parallel to the beam at 15 kV and 5 nA.

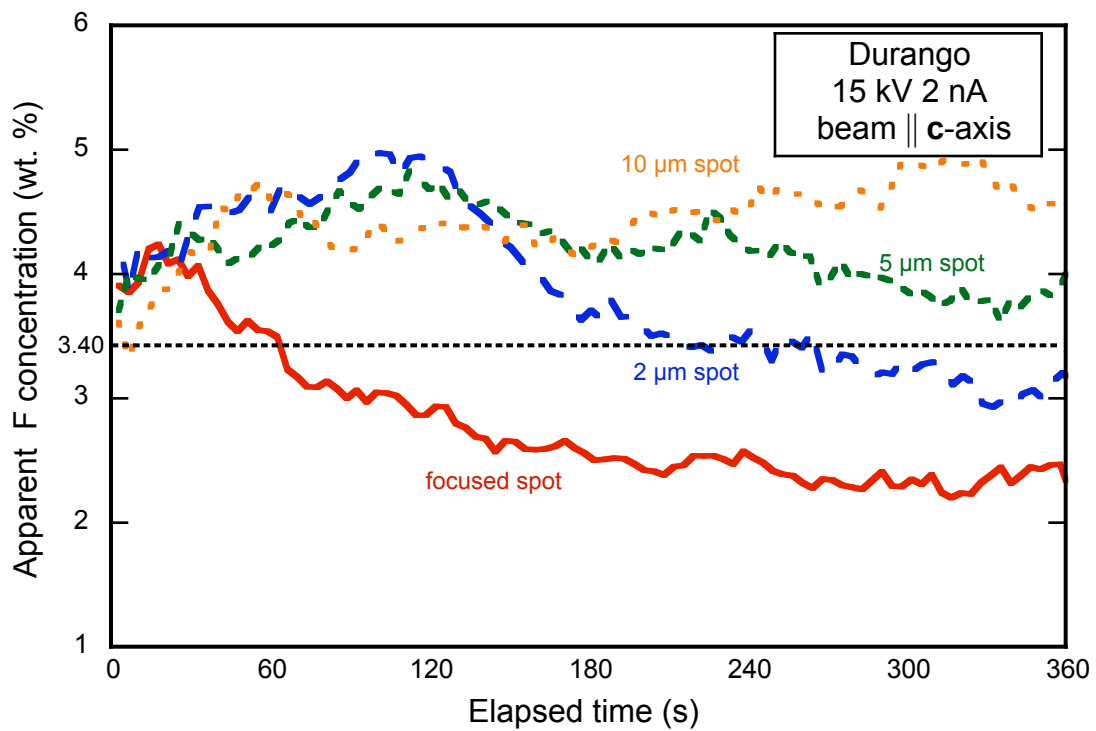


**Figure 1d.** Apparent F concentration with time for different beam spot sizes measured on Durango apatite oriented with the c-axis parallel to the beam at 15 kV and 2 nA.

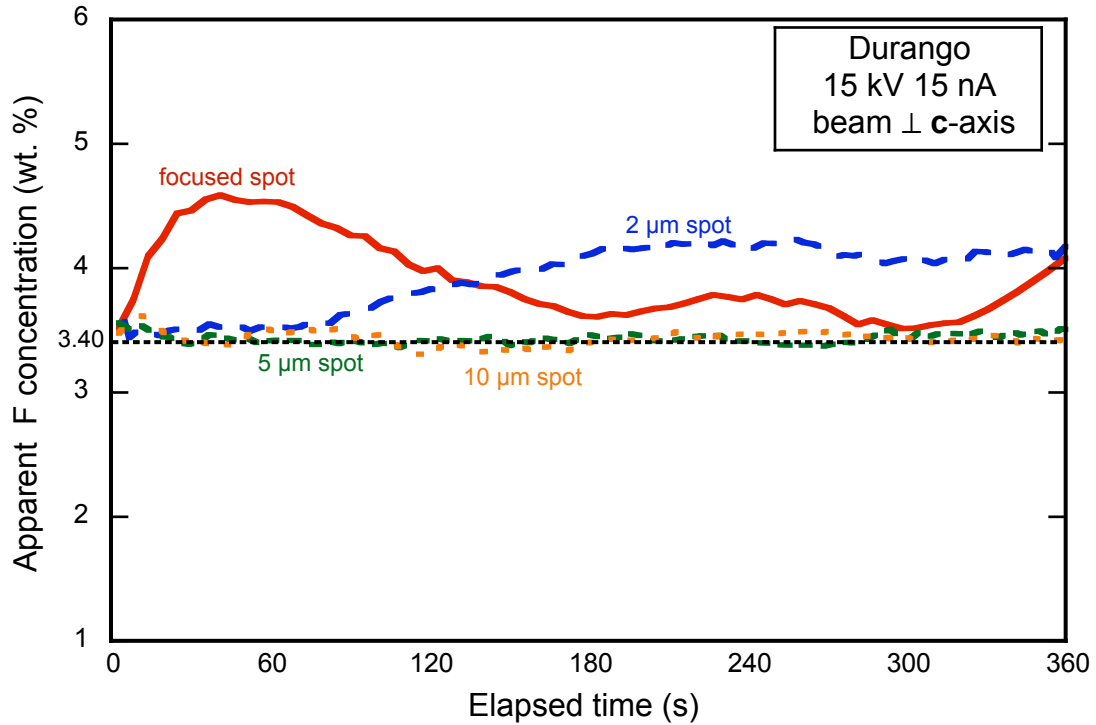


**Figure 2a.** Apparent F concentration with time for different beam spot sizes measured on Durango apatite oriented with the c-axis perpendicular to the beam at 15 kV and 15 nA.

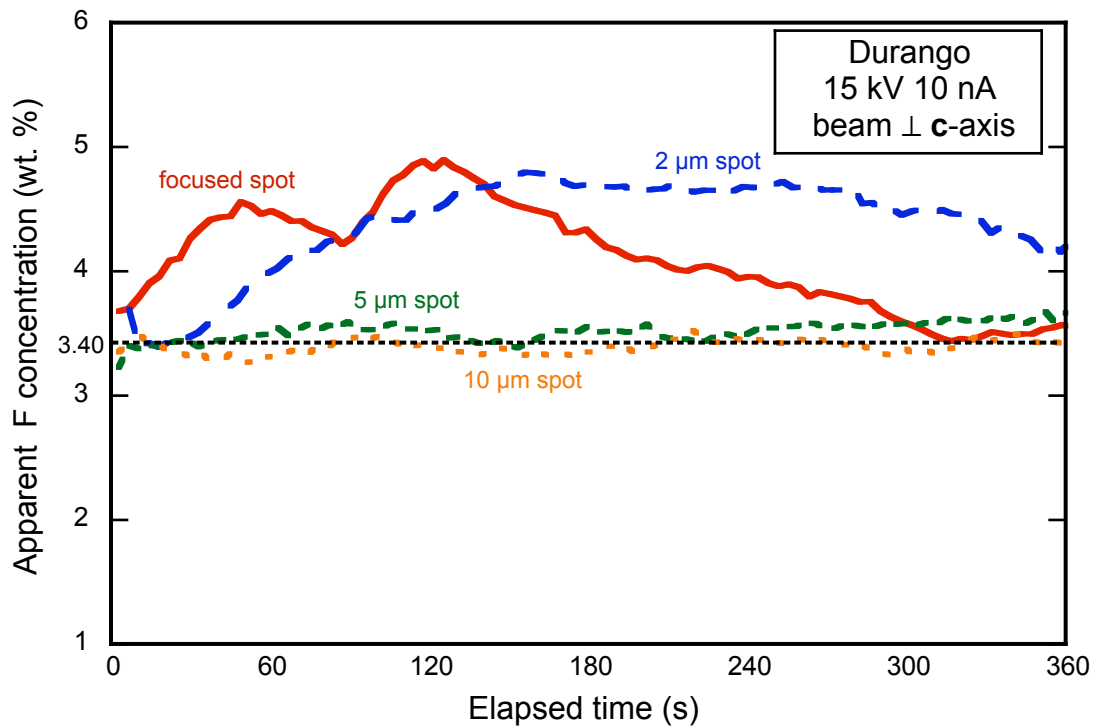


**Figure 2b.** Apparent F concentration with time for different beam spot sizes measured on Durango apatite oriented with the c-axis perpendicular to the beam at 15 kV and 10 nA.

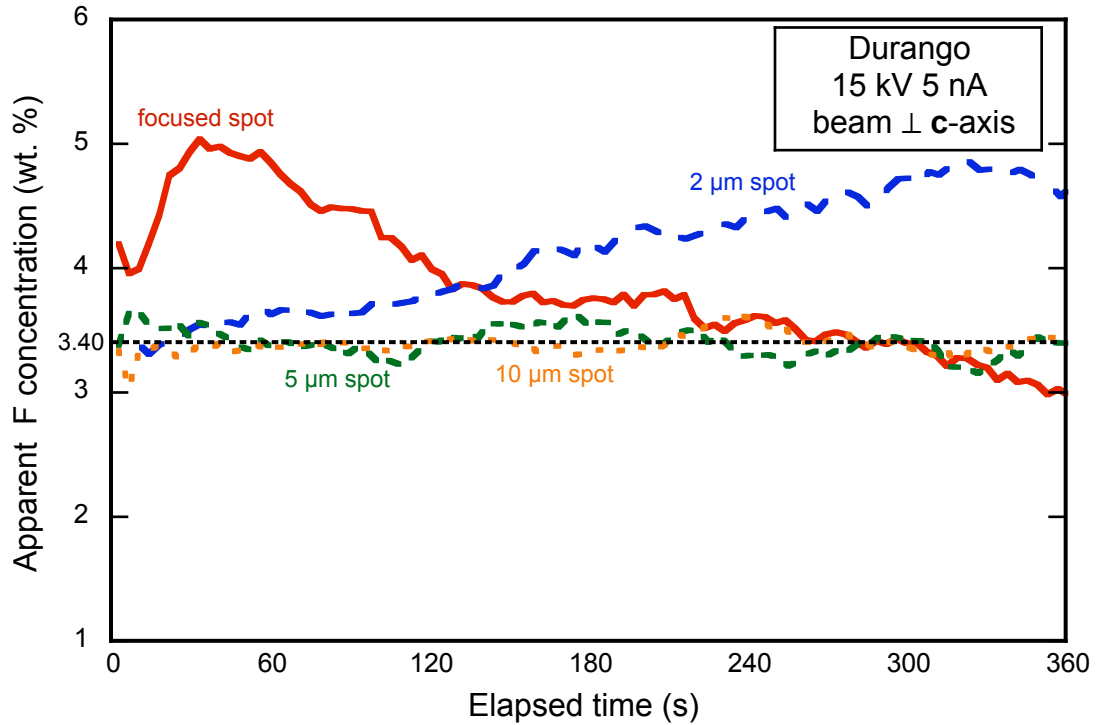


**Figure 2c.** Apparent F concentration with time for different beam spot sizes measured on Durango apatite oriented with the **c**-axis perpendicular to the beam at 15 kV and 5 nA.

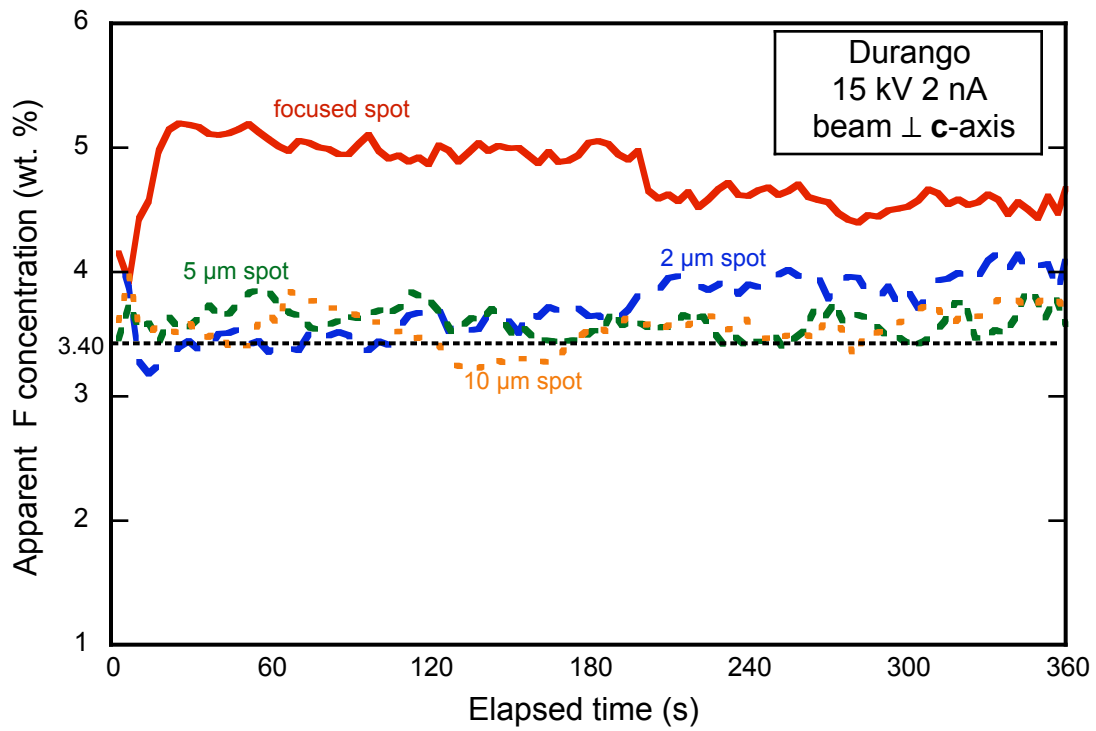


**Figure 2d.** Apparent F concentration with time for different beam spot sizes measured on Durango apatite oriented with the **c**-axis perpendicular to the beam at 15 kV and 2 nA.

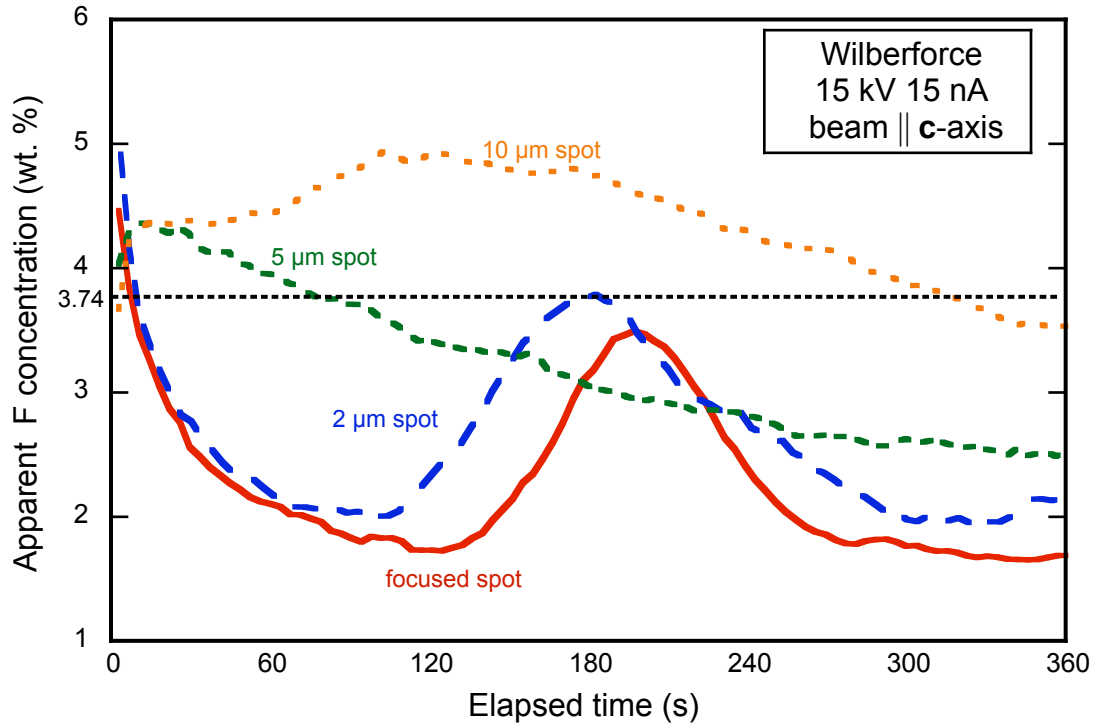


**Figure 3a.** Apparent F concentration with time for different beam spot sizes measured on Wilberforce apatite oriented with the **c**-axis parallel to the electron beam at 15 kV and 15 nA.

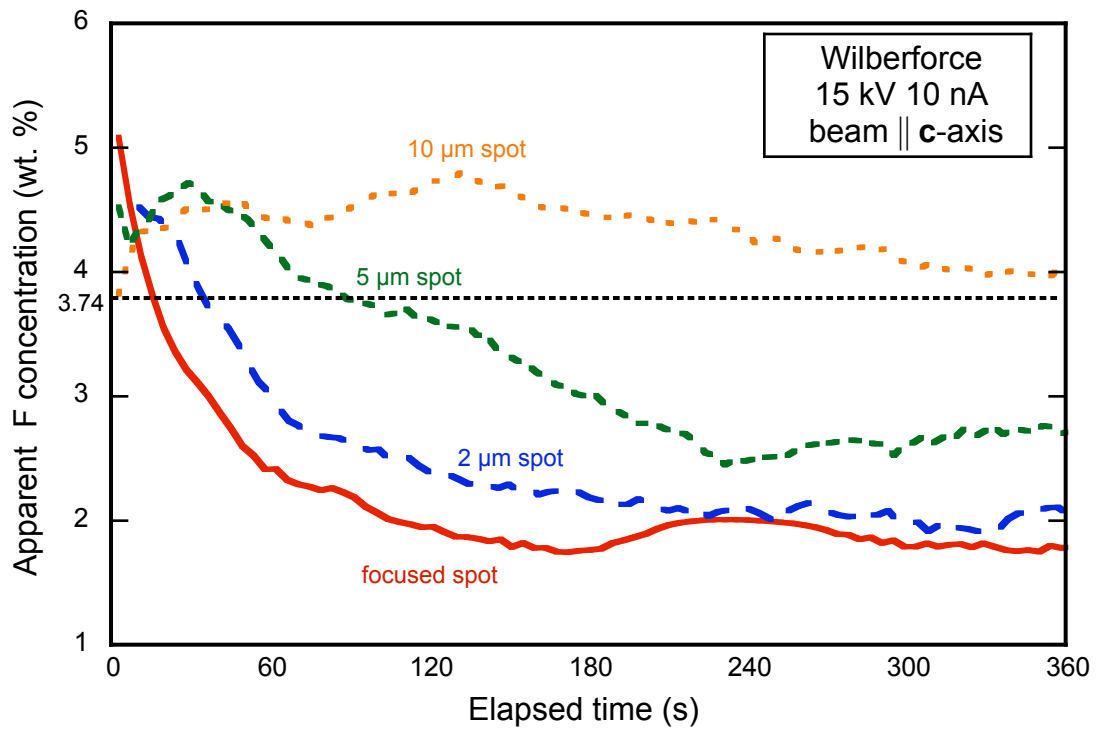


**Figure 3b.** Apparent F concentration with time for different beam spot sizes measured on Wilberforce apatite oriented with the **c**-axis parallel to the electron beam at 15 kV and 10 nA.

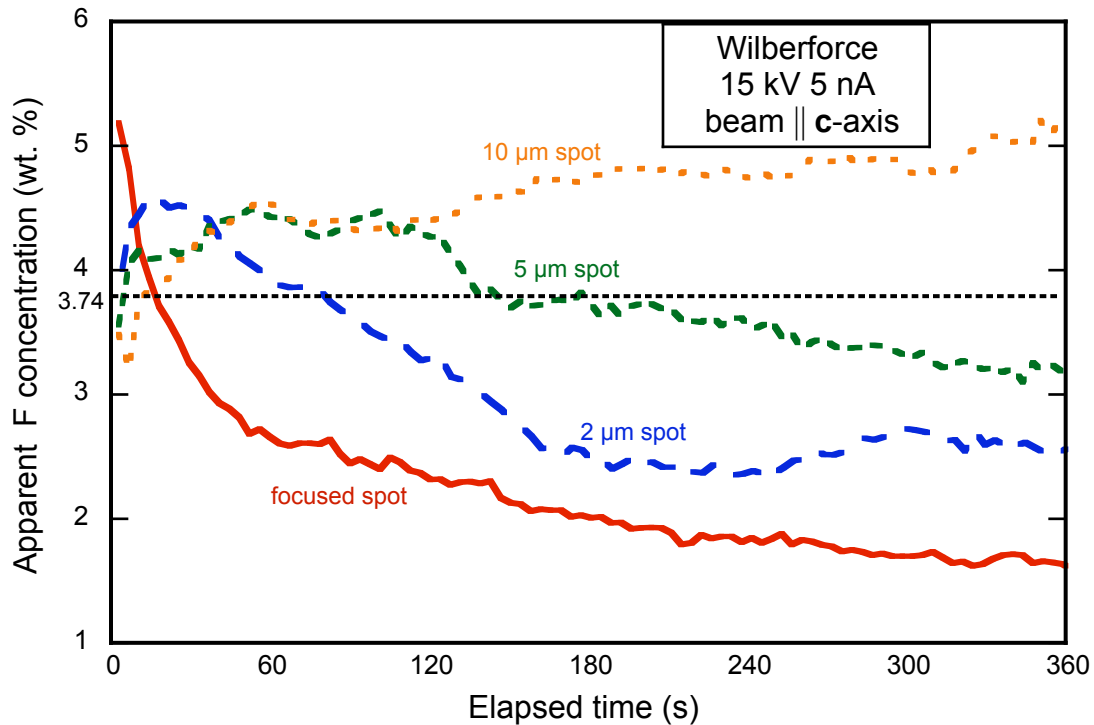


**Figure 3c.** Apparent F concentration with time for different beam spot sizes measured on Wilberforce apatite oriented with the c-axis parallel to the electron beam at 15 kV and 5 nA.

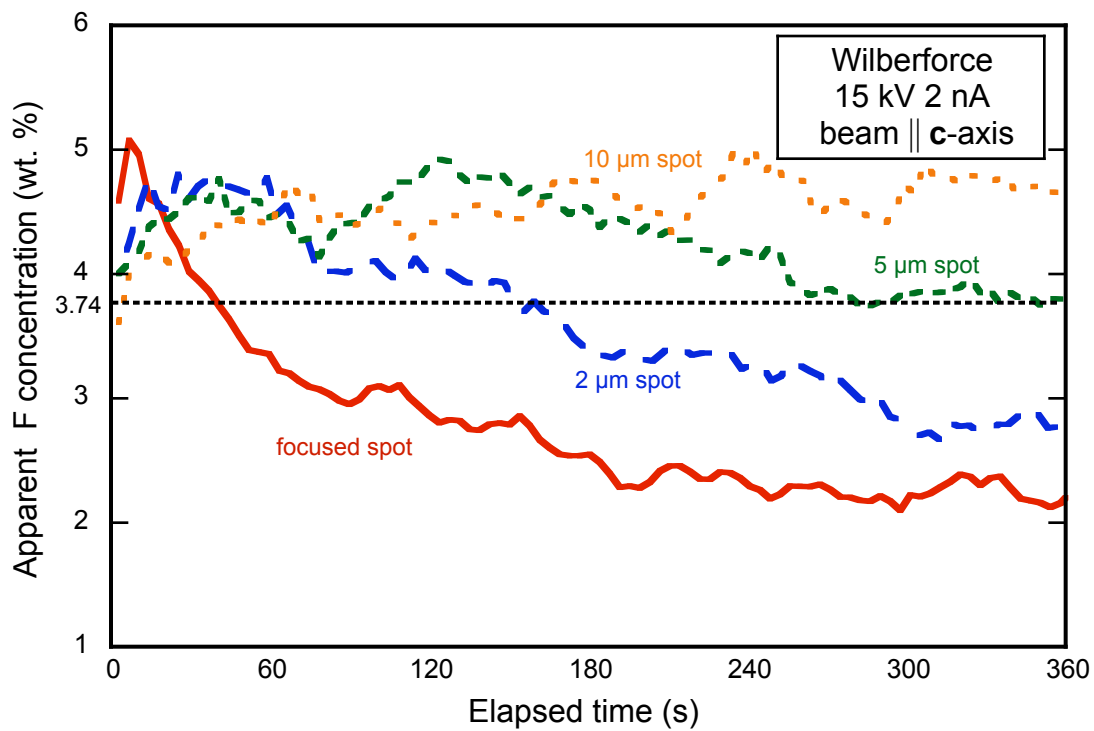


**Figure 3d.** Apparent F concentration with time for different beam spot sizes measured on Wilberforce apatite oriented with the c-axis parallel to the electron beam at 15 kV and 2 nA.

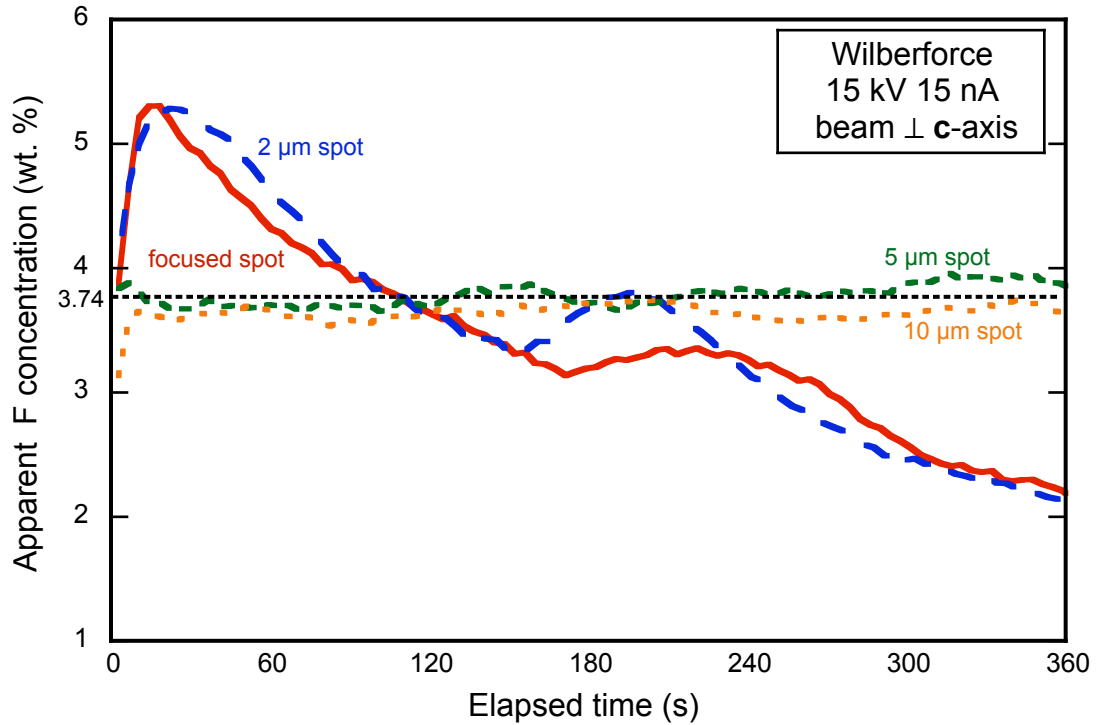


**Figure 4a.** Apparent F concentration with time for different beam spot sizes measured on Wilberforce apatite oriented with the c-axis perpendicular to the beam at 15 kV and 15 nA.

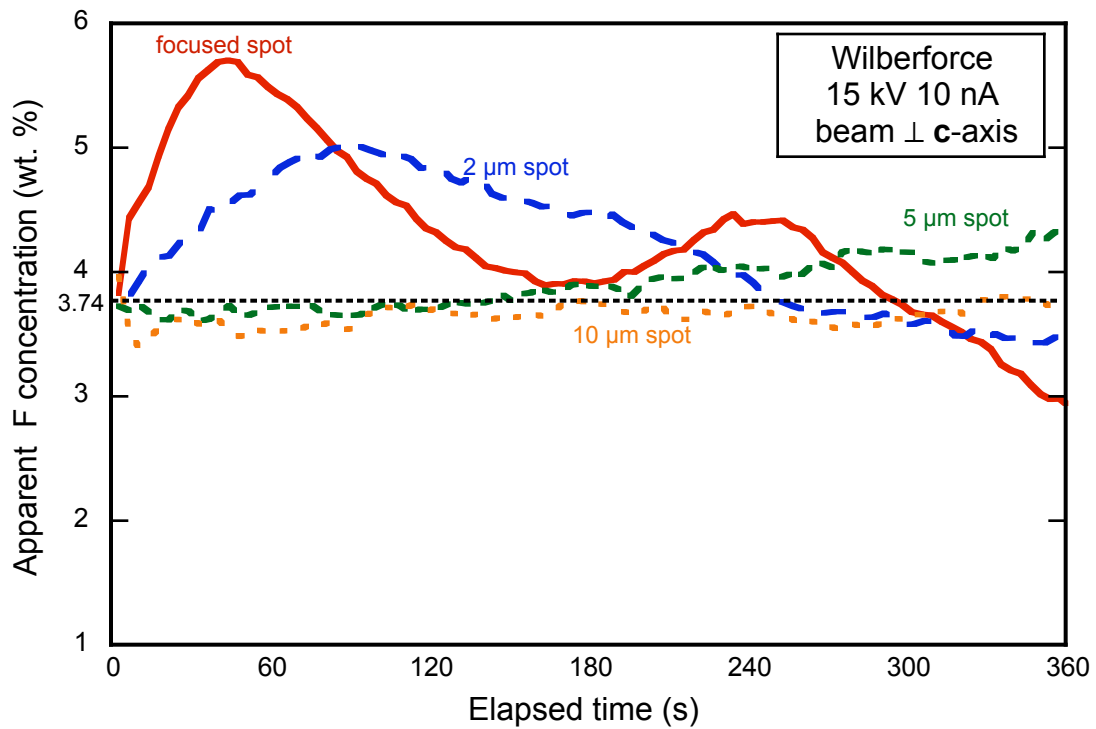


**Figure 4b.** Apparent F concentration with time for different beam spot sizes measured on Wilberforce apatite oriented with the c-axis perpendicular to the beam at 15 kV and 10 nA.



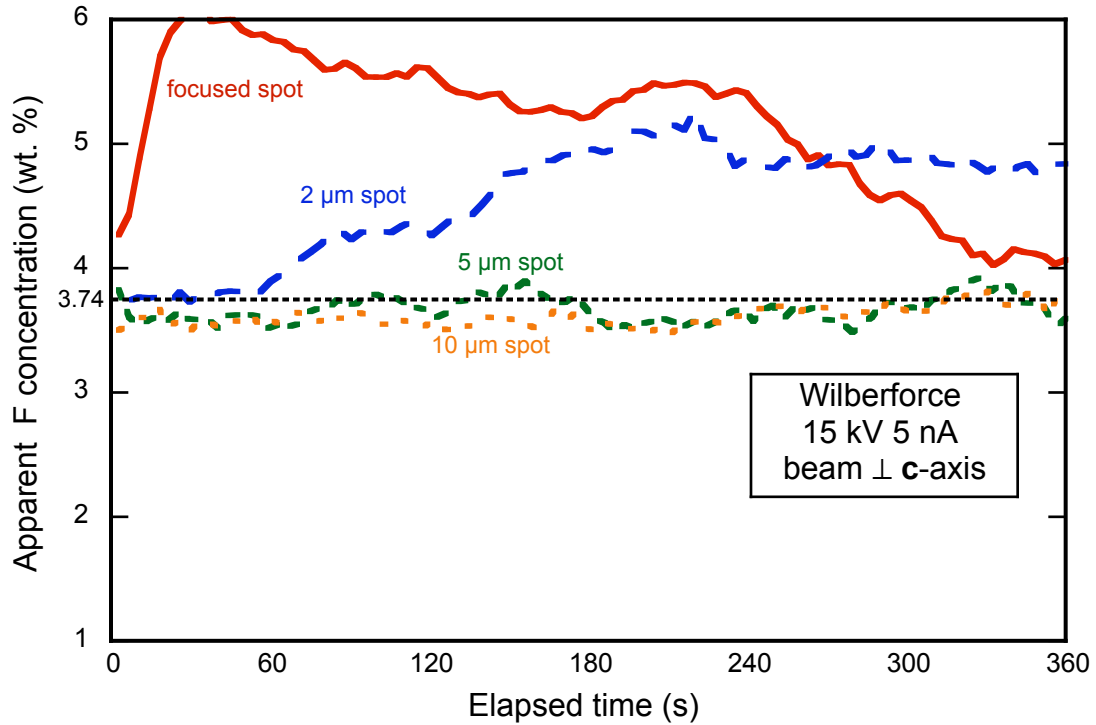


**Figure 4c.** Apparent F concentration with time for different beam spot sizes measured on Wilberforce apatite oriented with the **c**-axis perpendicular to the beam at 15 kV and 10 nA.

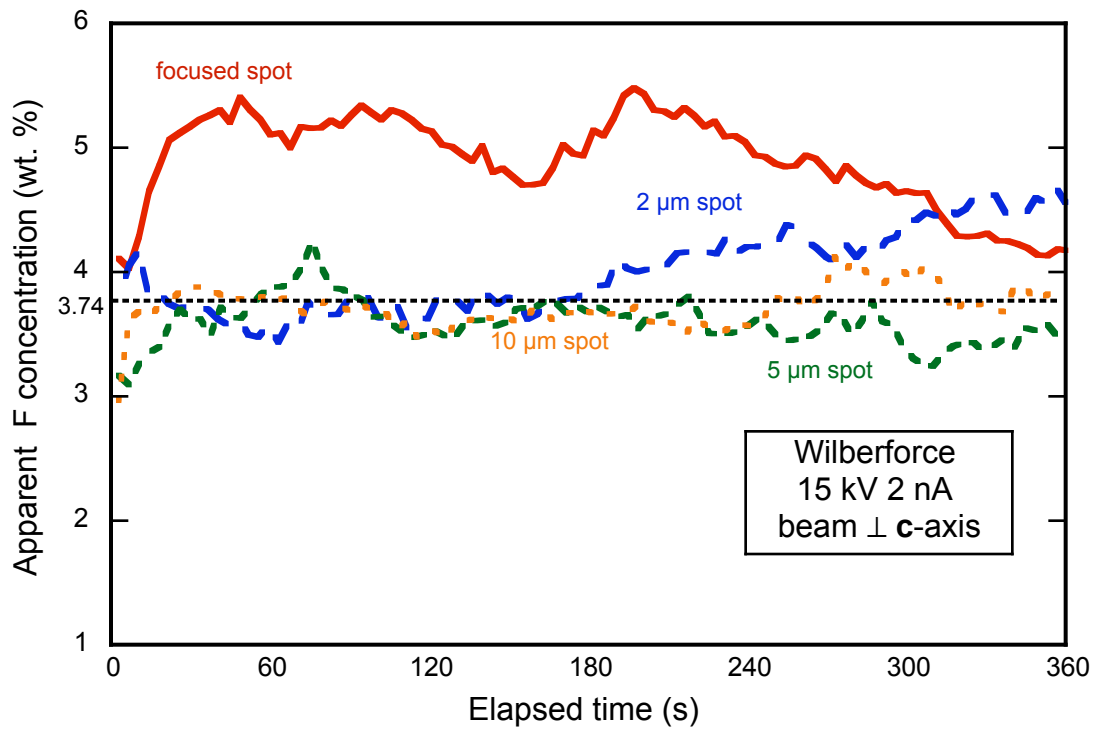


**Figure 4d.** Apparent F concentration with time for different beam spot sizes measured on Wilberforce apatite oriented with the **c**-axis perpendicular to the beam at 15 kV and 10 nA.

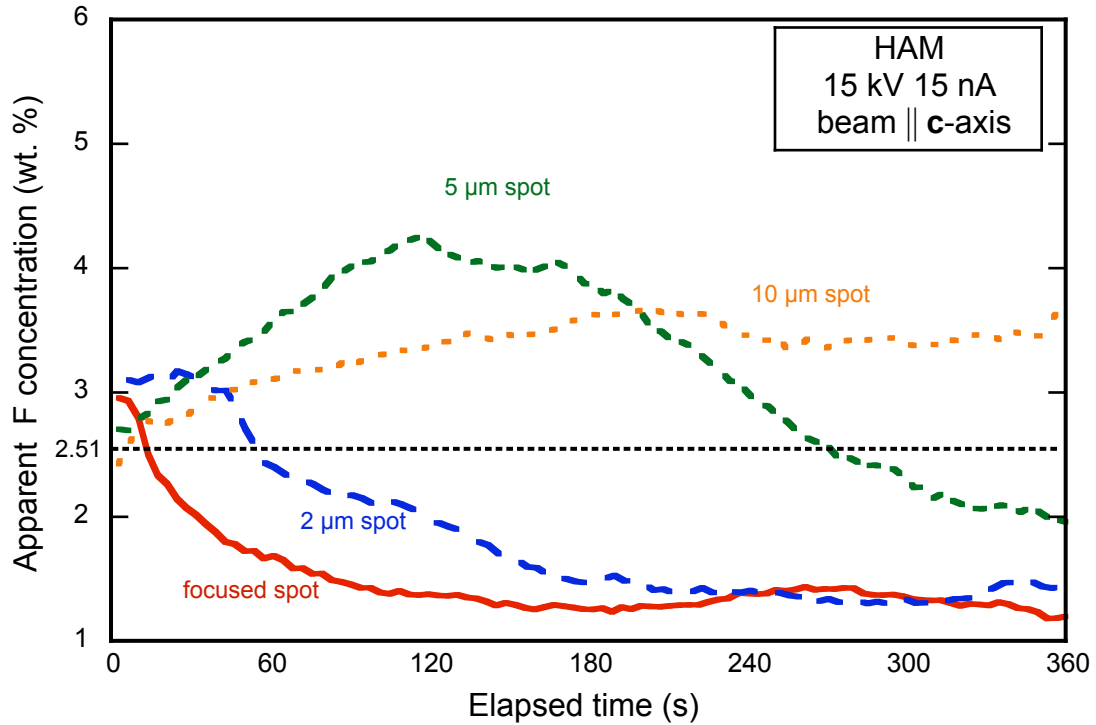


**Figure 5a.** Apparent F concentration with time for different beam spot sizes measured on High Atlas Mountains apatite oriented with the *c*-axis parallel to the beam at 15 kV and 15 nA.

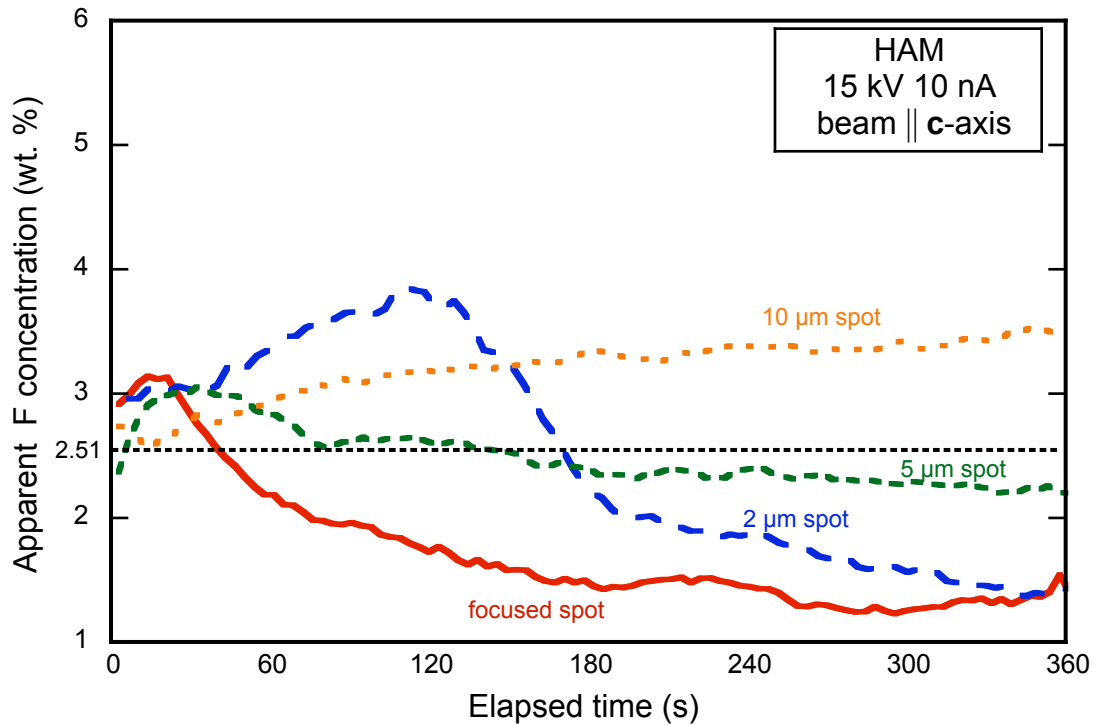


**Figure 5b.** Apparent F concentration with time for different beam spot sizes measured on High Atlas Mountains apatite oriented with the *c*-axis parallel to the beam at 15 kV and 10 nA.

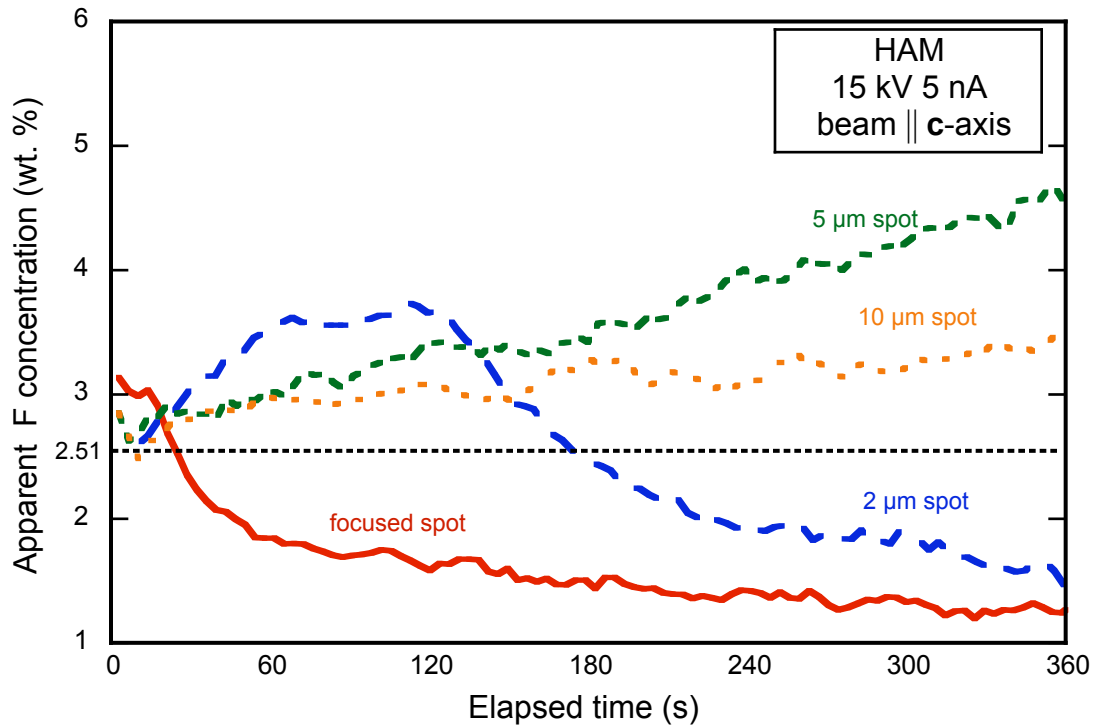


**Figure 5c.** Apparent F concentration with time for different beam spot sizes measured on High Atlas Mountains apatite oriented with the c-axis parallel to the beam at 15 kV and 5 nA.

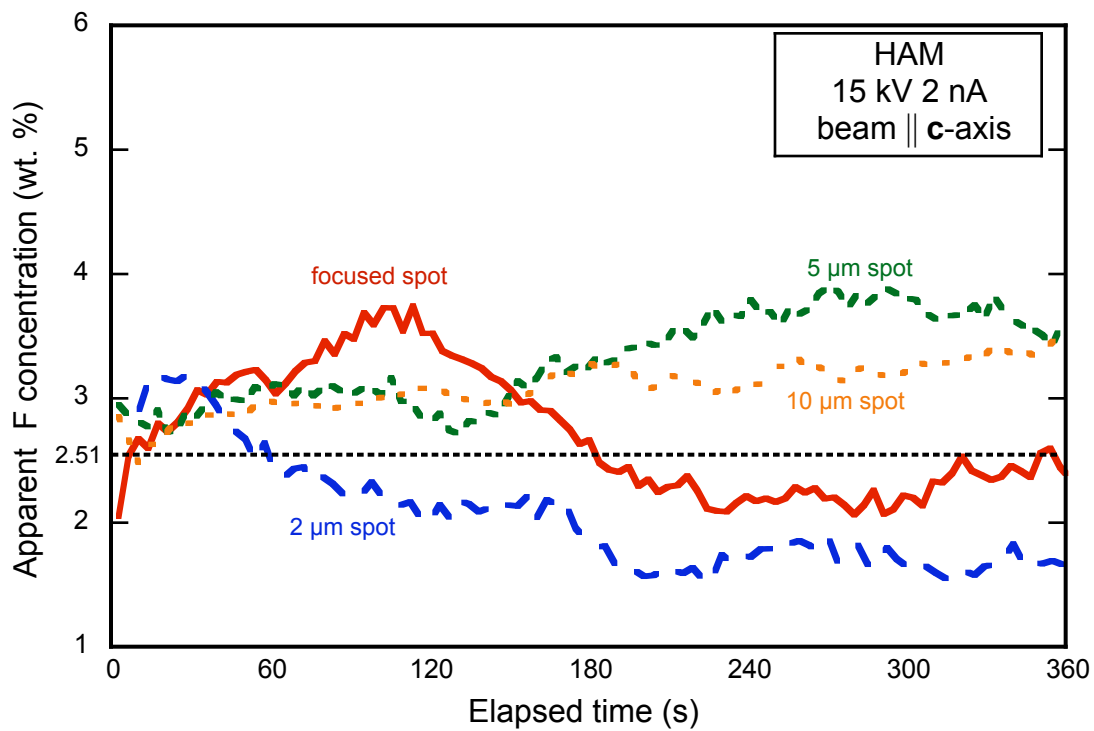


**Figure 5d.** Apparent F concentration with time for different beam spot sizes measured on High Atlas Mountains apatite oriented with the c-axis parallel to the beam at 15 kV and 2 nA.

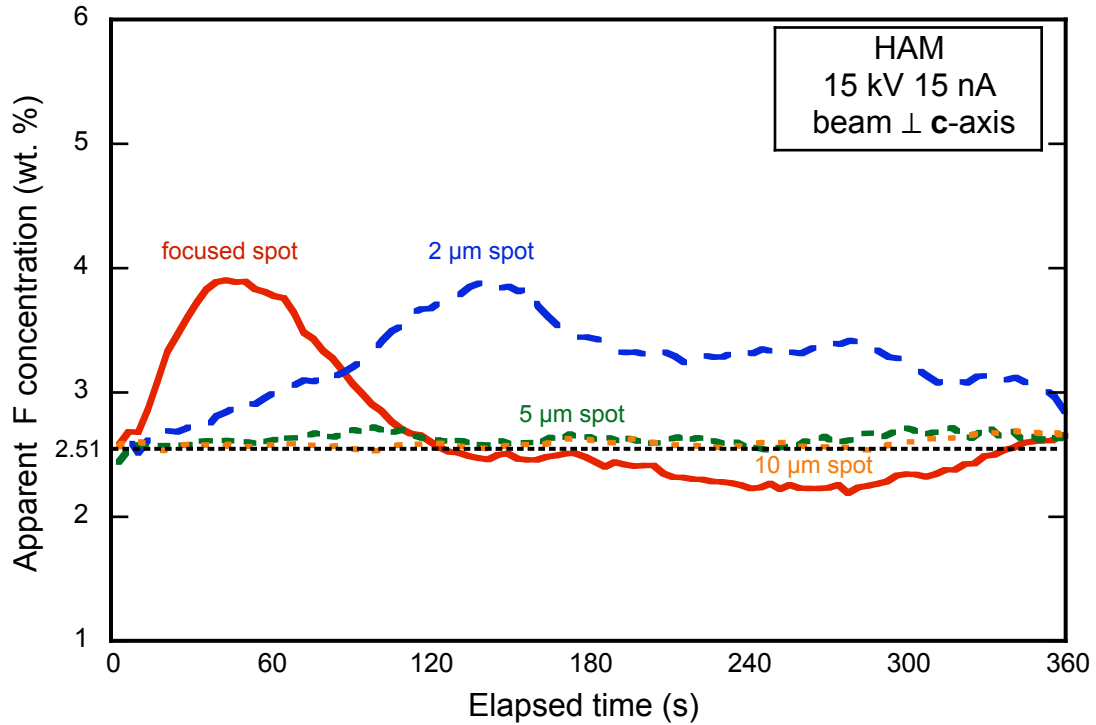


**Figure 6a.** Apparent F concentration with time for different beam spot sizes measured on High Atlas Mountains apatite oriented with the **c**-axis perpendicular to the beam at 15 kV and 15 nA.

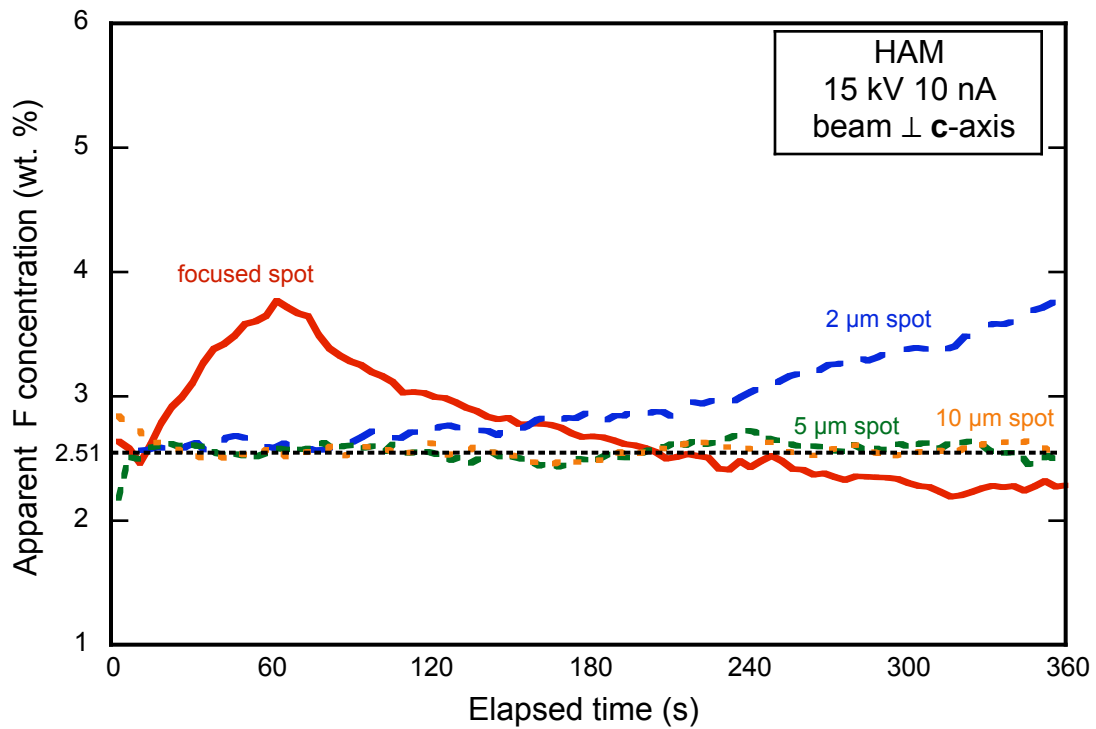


**Figure 6b.** Apparent F concentration with time for different beam spot sizes measured on High Atlas Mountains apatite oriented with the **c**-axis perpendicular to the beam at 15 kV and 10 nA.

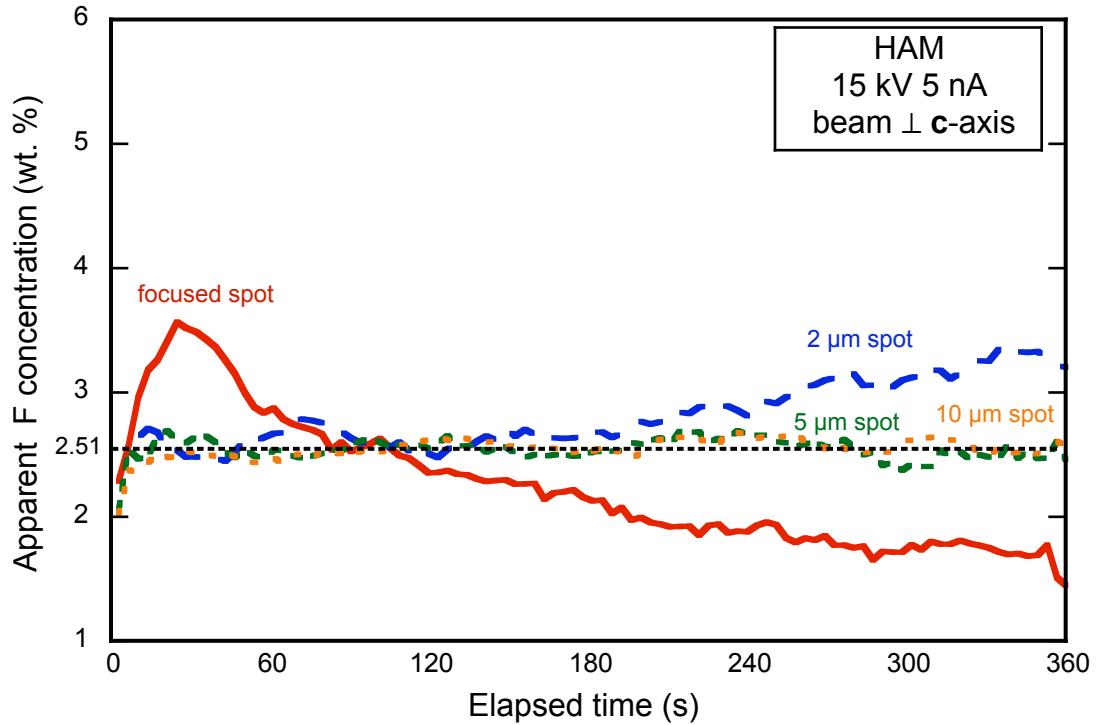


**Figure 6c.** Apparent F concentration with time for different beam spot sizes measured on High Atlas Mountains apatite oriented with the *c*-axis perpendicular to the beam at 15 kV and 5 nA.

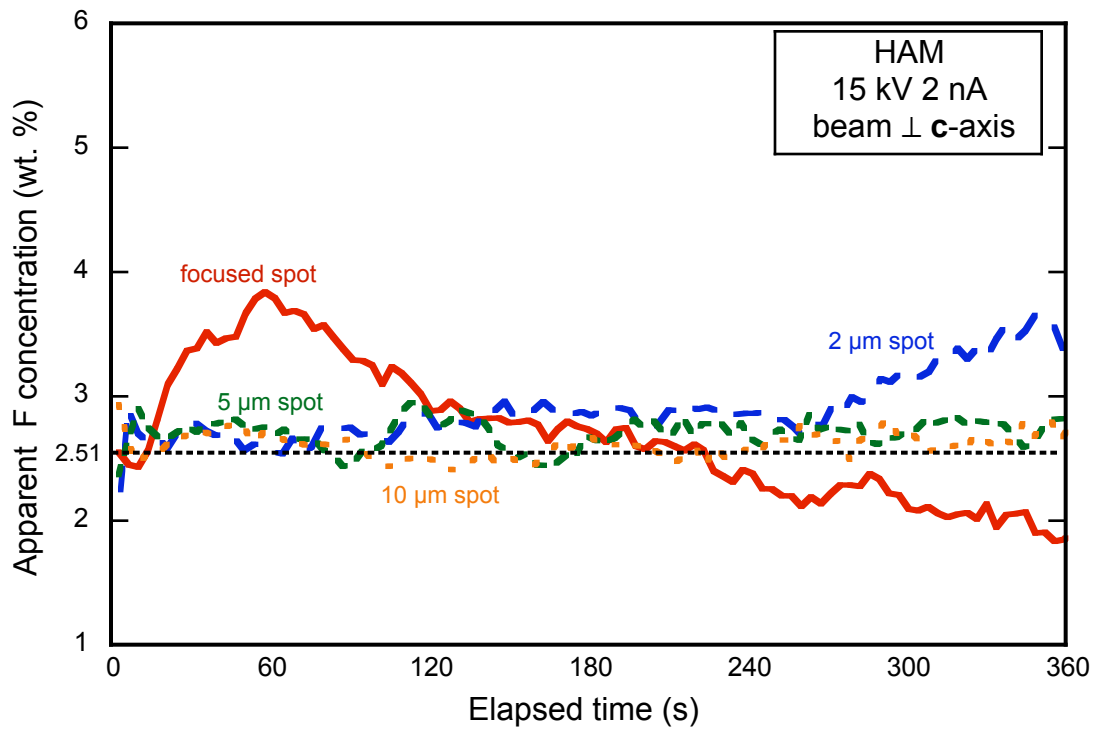


**Figure 6d.** Apparent F concentration with time for different beam spot sizes measured on High Atlas Mountains apatite oriented with the *c*-axis perpendicular to the beam at 15 kV and 2 nA.

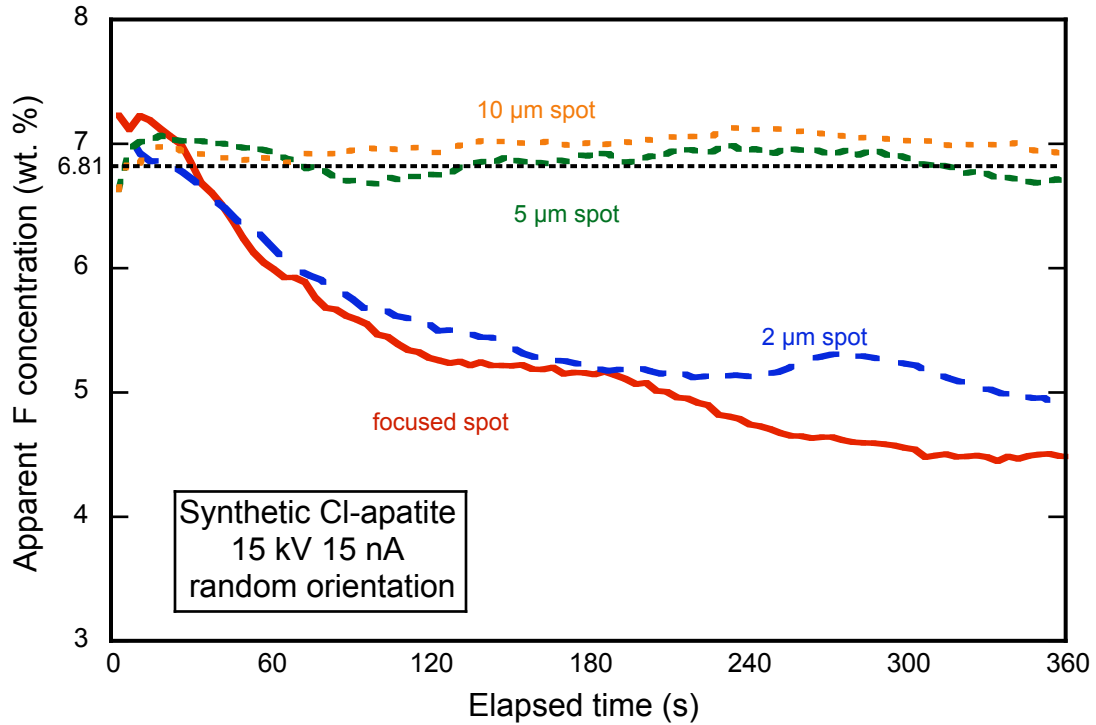


**Figure 7a.** Apparent F concentration with time for different beam spot sizes measured on synthetic chlorapatite at 15 kV and 15 nA. The nominal composition is 6.81 wt. % Cl.

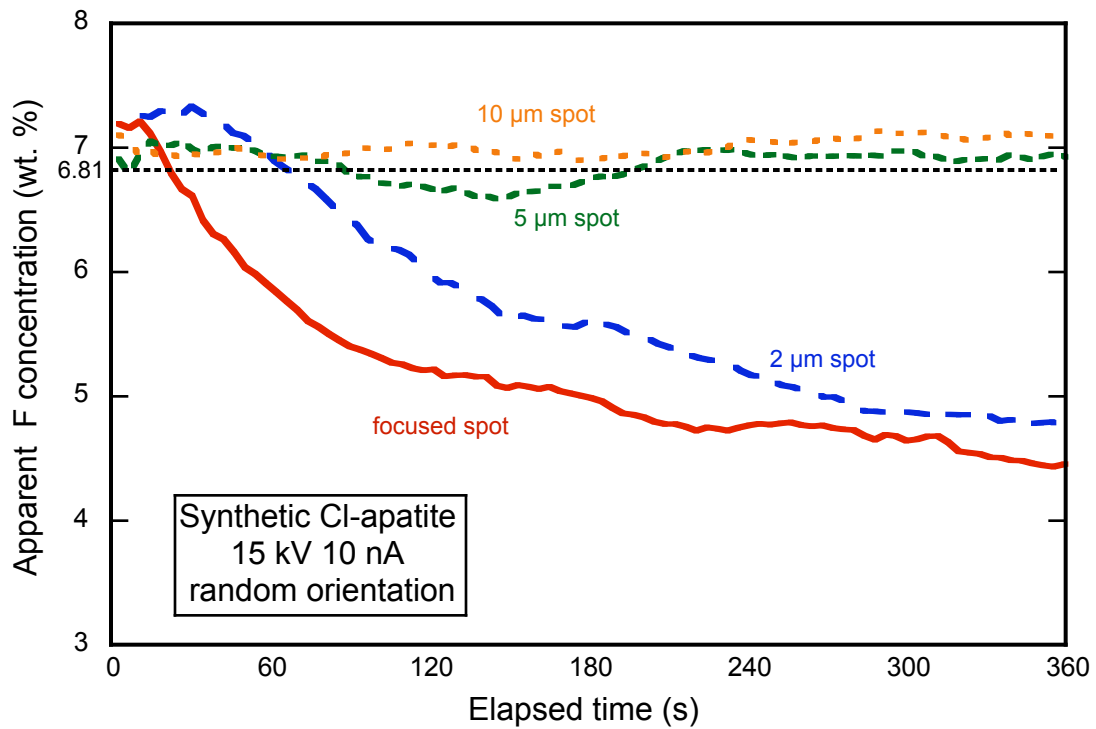


**Figure 7b.** Apparent F concentration with time for different beam spot sizes measured on synthetic chlorapatite at 15 kV and 10 nA. The nominal composition is 6.81 wt. % Cl.

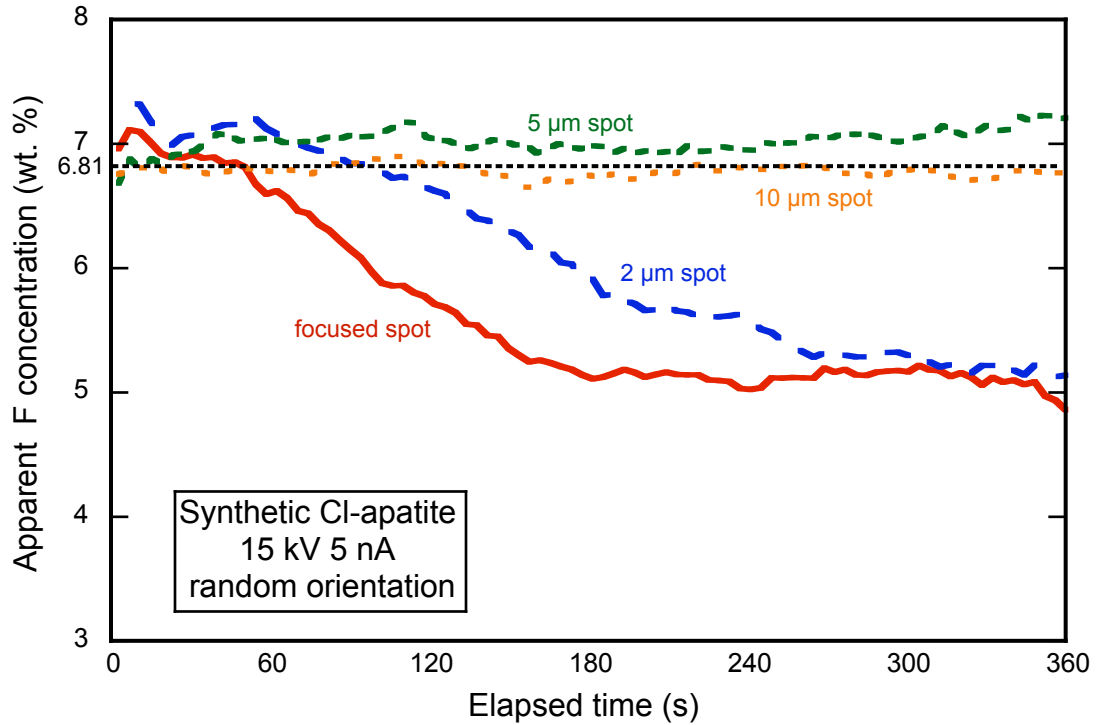


**Figure 7c.** Apparent Cl concentration with time for different beam spot sizes measured on synthetic chlorapatite at 15 kV and 5 nA. The nominal composition is 6.81 wt. % Cl.

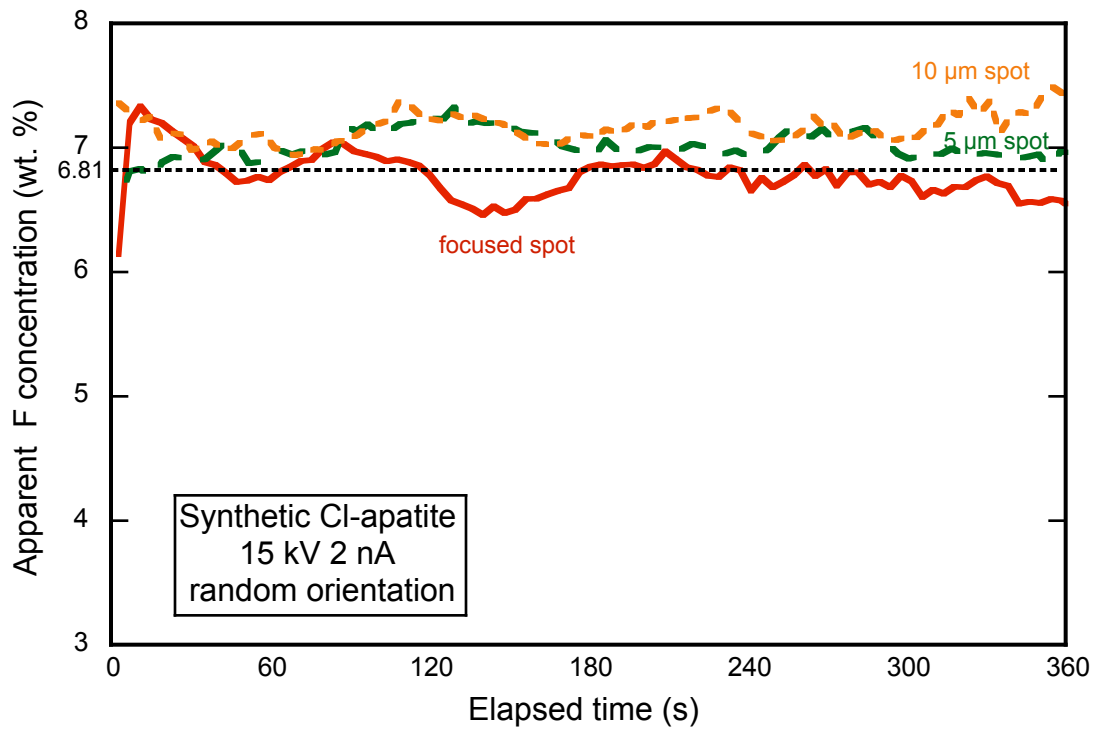


**Figure 7c.** Apparent Cl concentration with time for different beam spot sizes measured on synthetic chlorapatite at 15 kV and 2 nA. The nominal composition is 6.81 wt. % Cl.

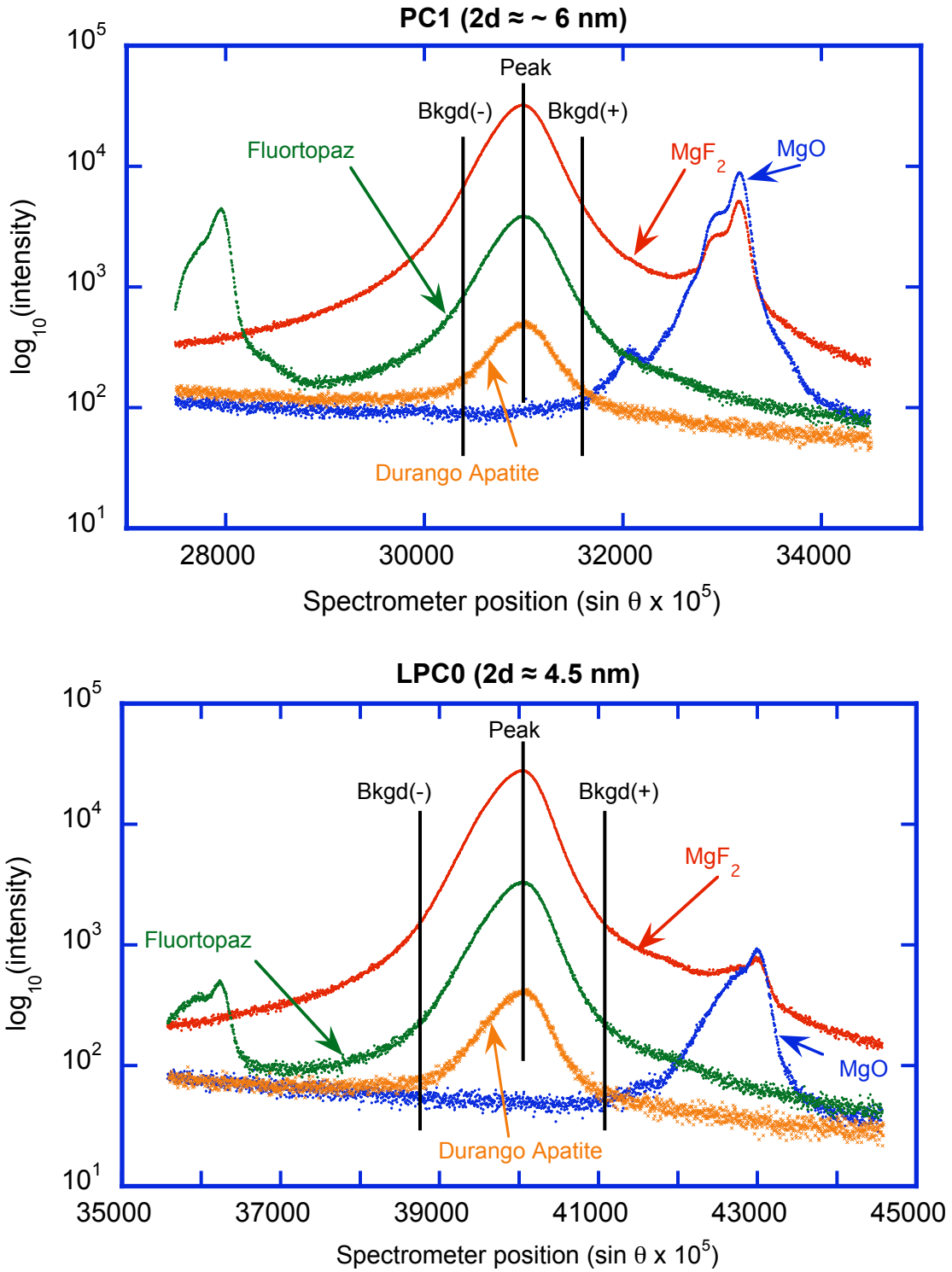


**Figure 8.** Wavelength dispersive spectrometer scans on LPC0 and PC1 LDEs in the region of the F K $\alpha$  peak, showing peak intensities, positions and shapes for materials evaluated for use as a F calibration standard.



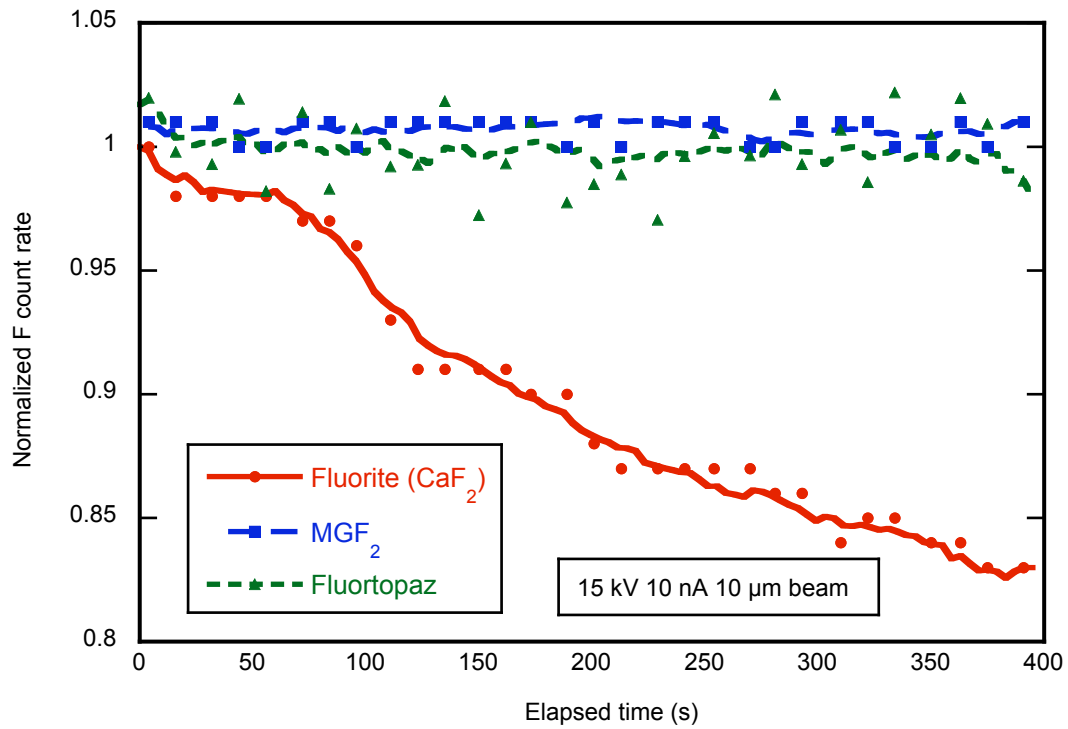


**Figure 9.** Normalized F count rates with time for materials evaluated for use as F calibration standards at the analytical condition of 15 kV, 10 nA and 10 μm diameter beam spot size.

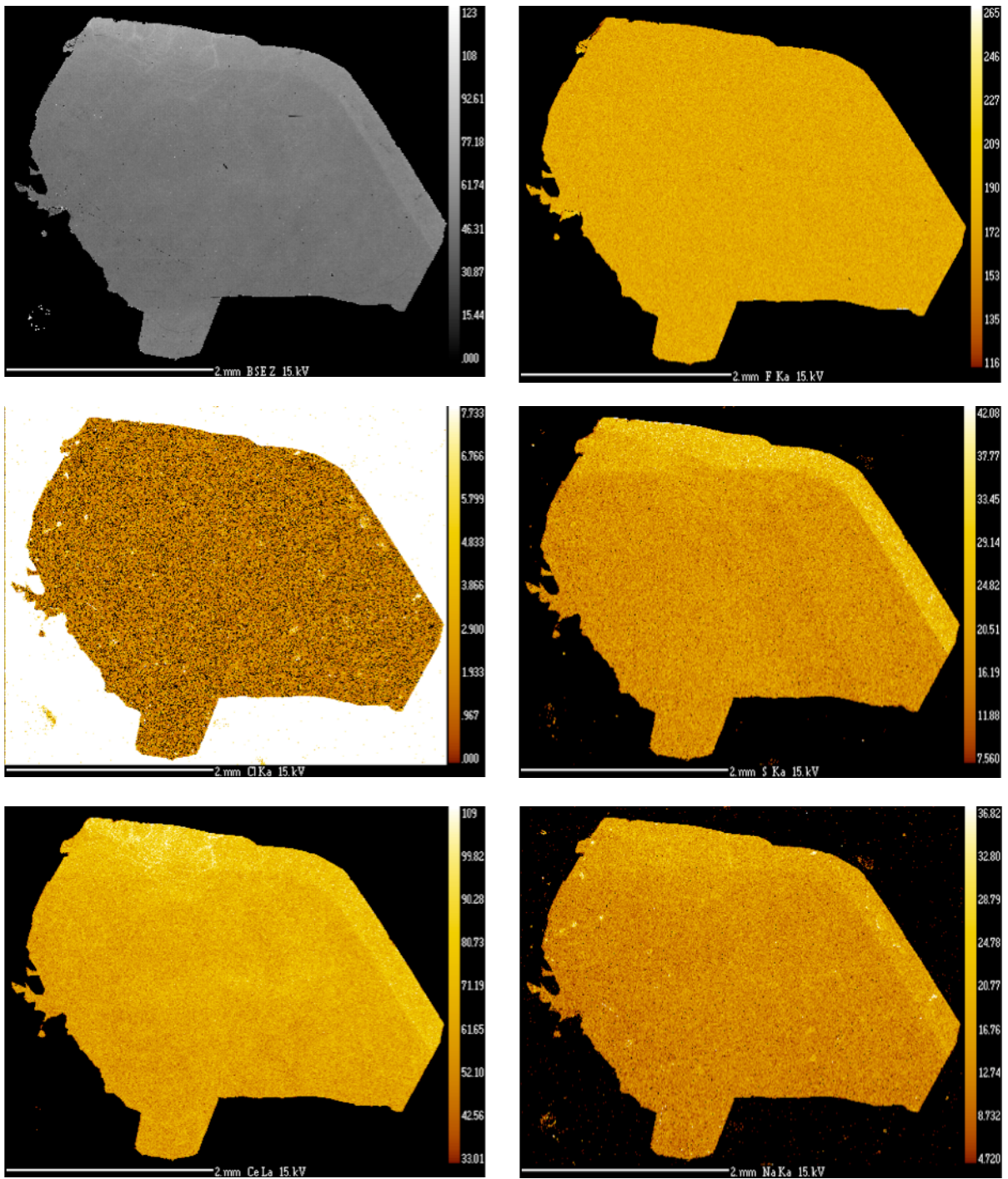


**Figure 10.** BEI and X-ray maps of Wilberforce apatite with c-axis normal to image plane. 15 kV, 50 nA, 180 ms dwell/pixel. Total acquisition time 4 hr. Embedding epoxy contains significant Cl.

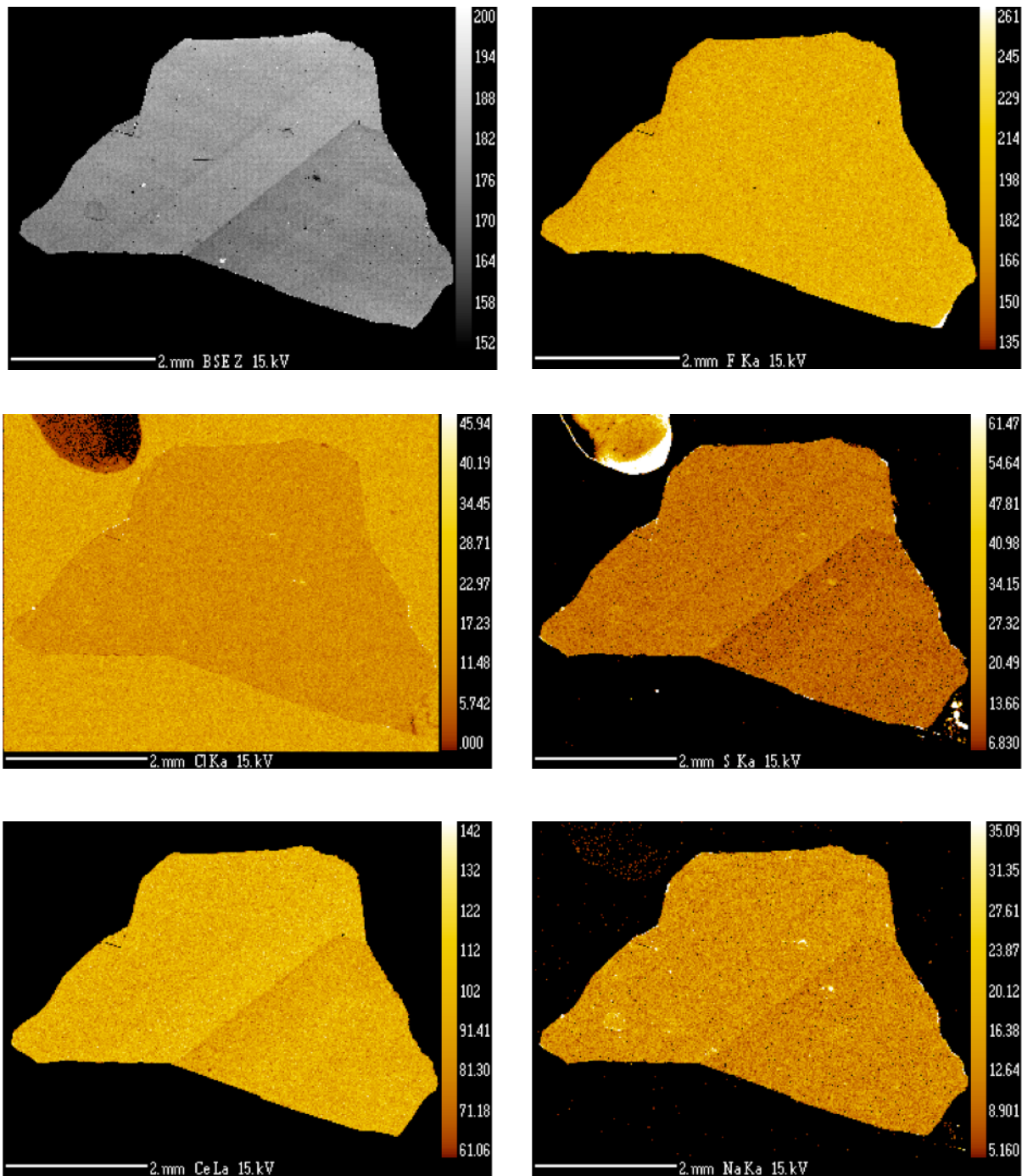


**Figure 11.** BEI and X-ray maps of Durango apatite with **c**-axis normal to the image plane. 15 kV, 50 nA, 180 ms dwell/pixel. Total acquisition time 4 hr. Embedding epoxy contains significant Cl.

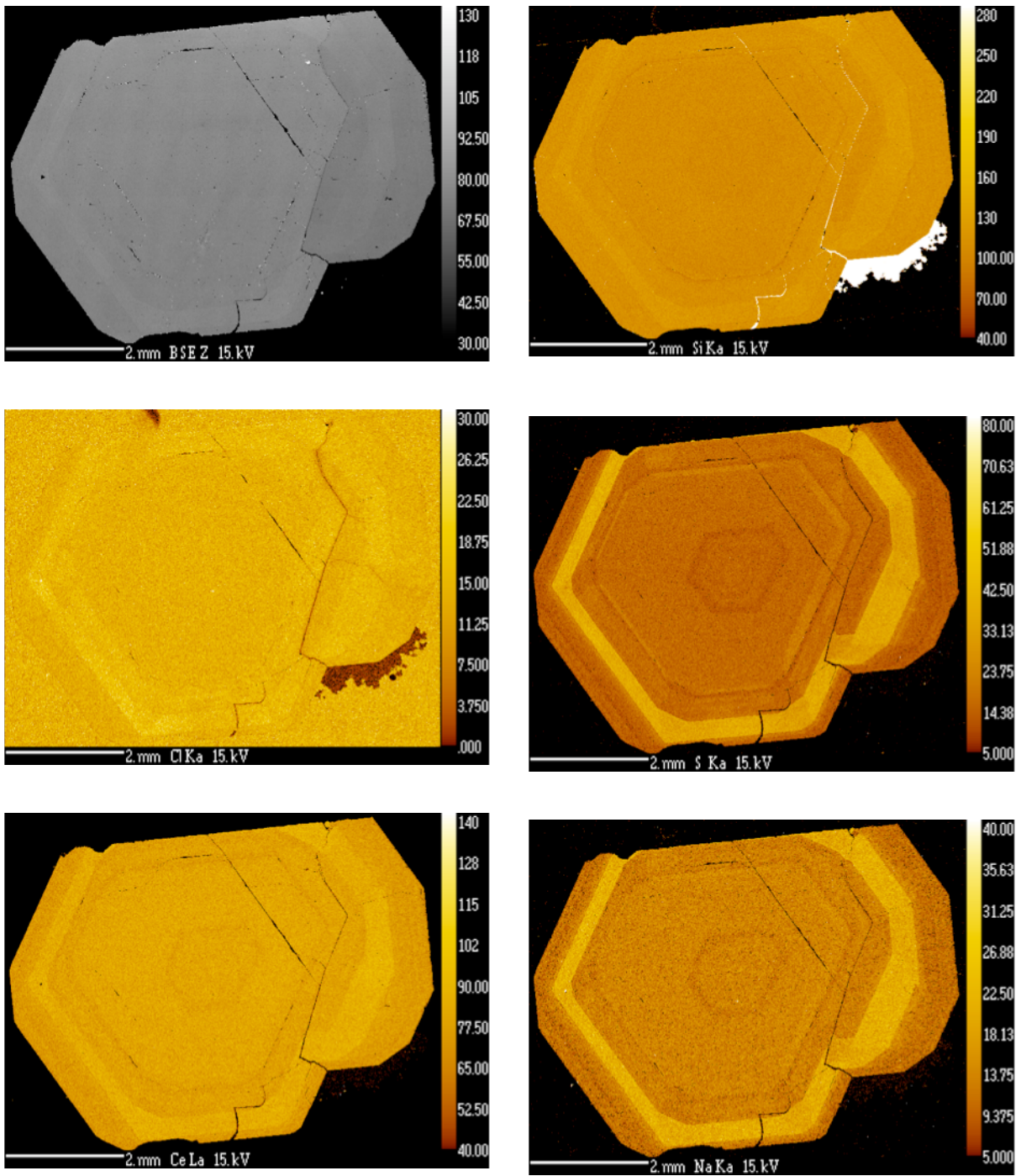


**Figure 12a.** BEI and X-ray maps of Durango apatite, Asparagus Stone sample, with *c*-axis perpendicular to image plane. 15 kV, 50 nA, 180 ms dwell/pixel. Total acquisition time 20 hr.

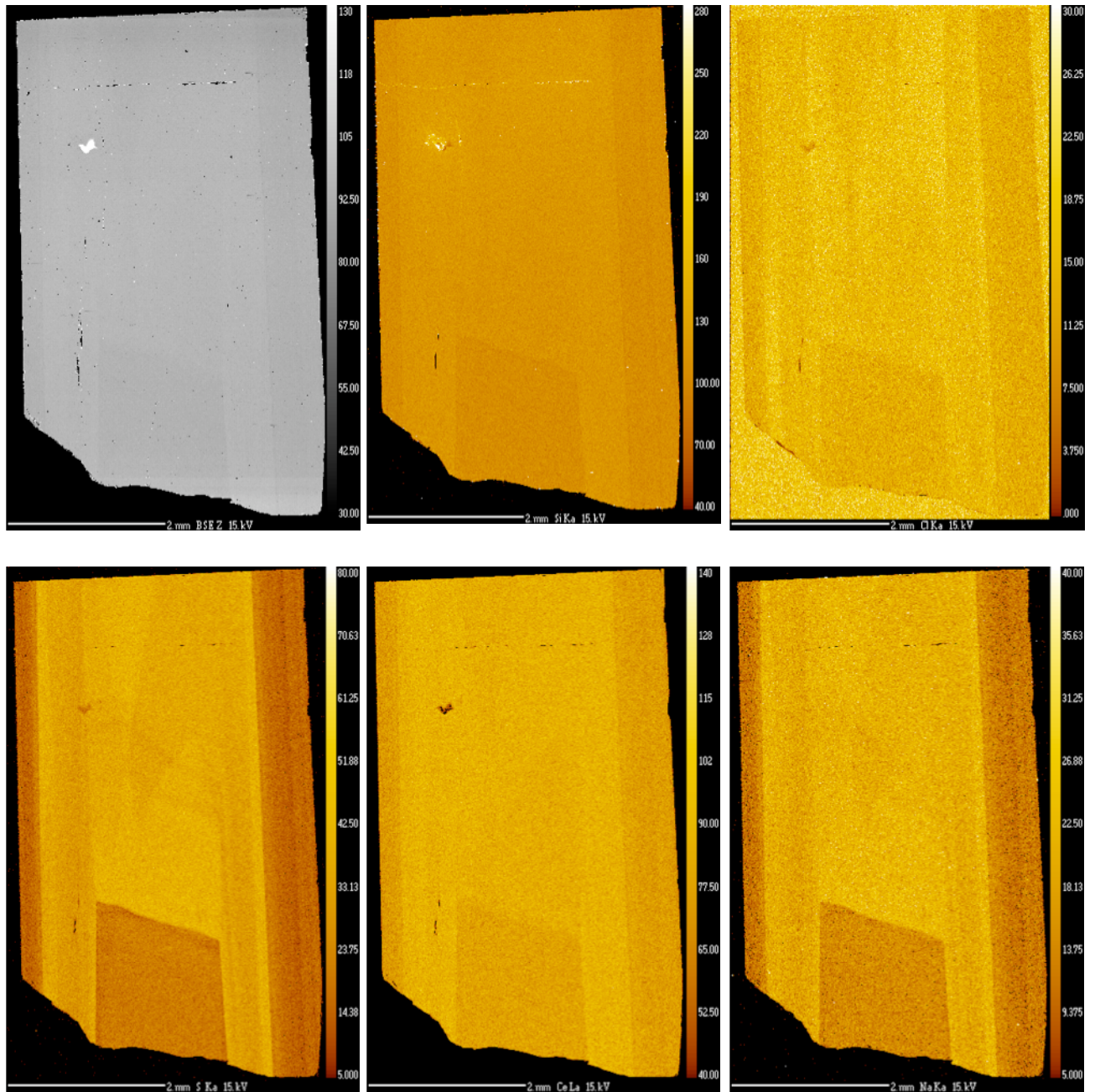


**Figure 12b.** BEI and X-ray mpas of Durango apatite, Asparagus Stone sample, with c-axis parallel to image plane. 15 kV, 50 nA, 180 ms dwell/pixel. Total acquisition time 10 hr.

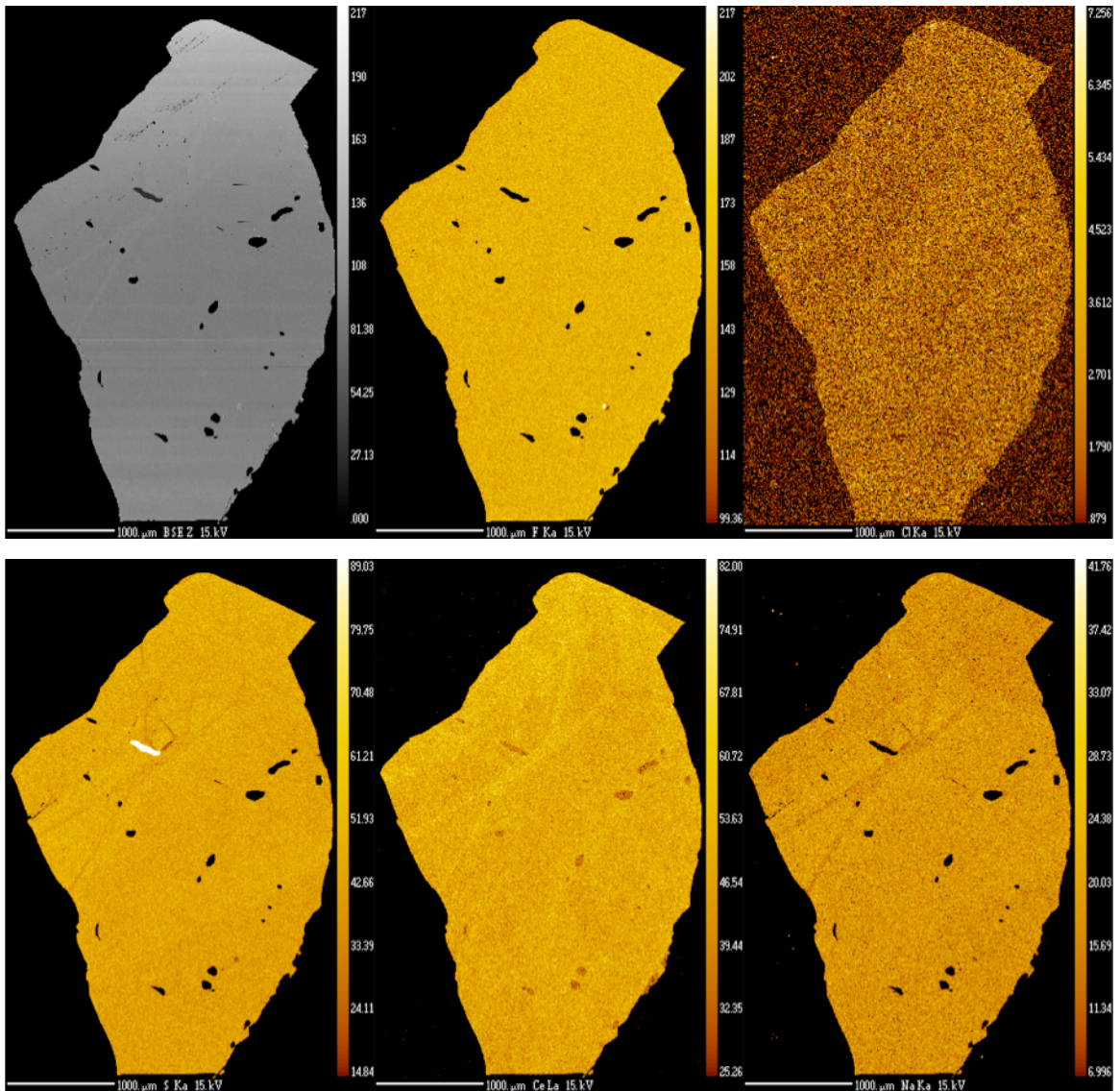


**Figure 13.** BEI and X-ray maps of Gem3 apatite with **c**-axis normal to image plane. 15 kV, 50 nA, 180 ms dwell/pixel. Total acquisition time 8 hr.

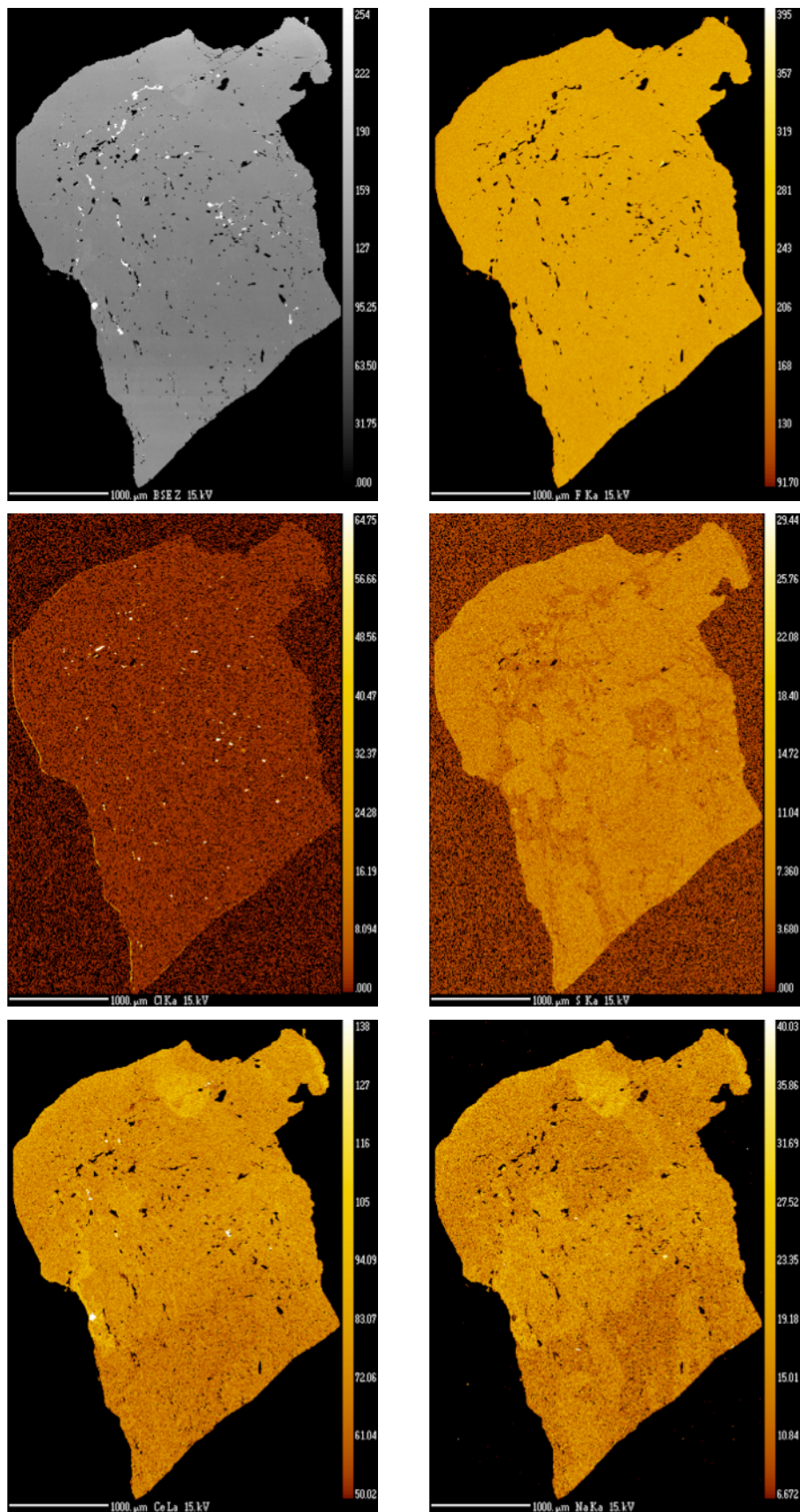


**Figure 14.** BEI and X-ray maps of Silver Crater Mine apatite with **c**-axis normal to image plane. 15 kV, 50 nA, 180 ms dwell/pixel. Total acquisition time 9 hr.

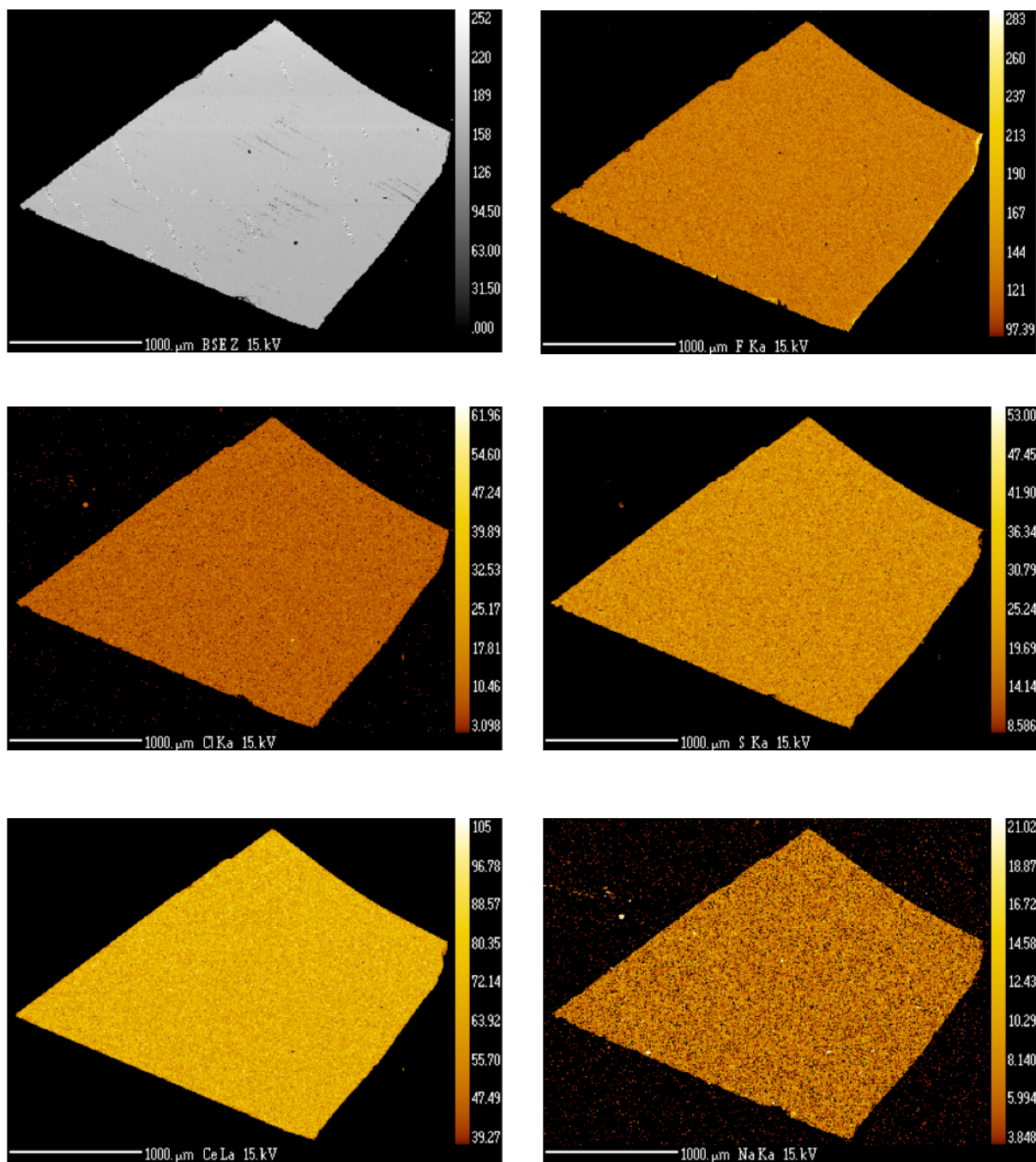


**Figure 15.** BEI and X-ray maps of High Atlas Mountains apatite with **c**-axis normal to image plane. 15 kV, 50 nA, 180 ms dwell/pixel. Total acquisition time 4.5 hr.



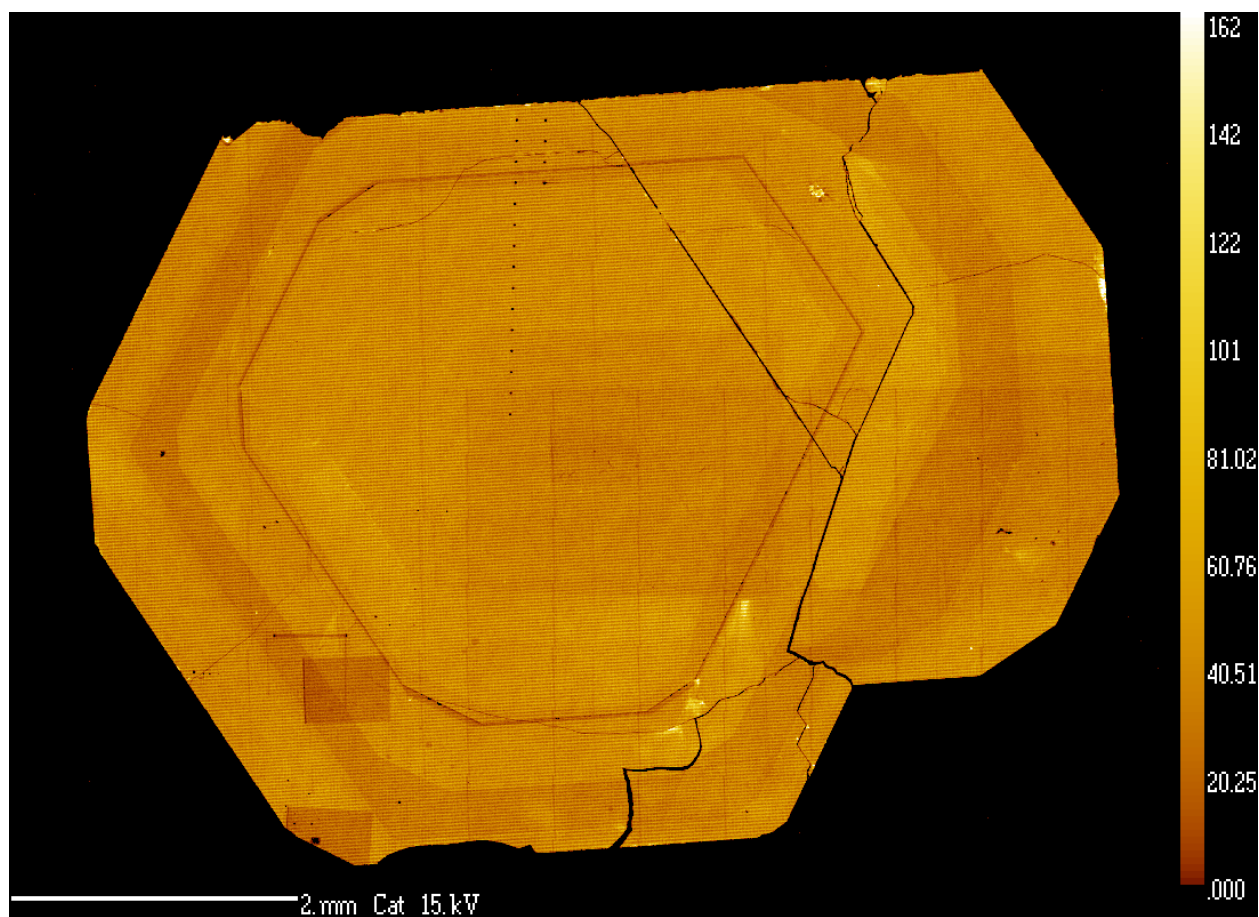


**Figure 16.** Mosaic panchromatic cathodoluminescence (CL) image of Durango apatite, Asparagus Stone sample. Crystallographic *c*-axis is vertical.

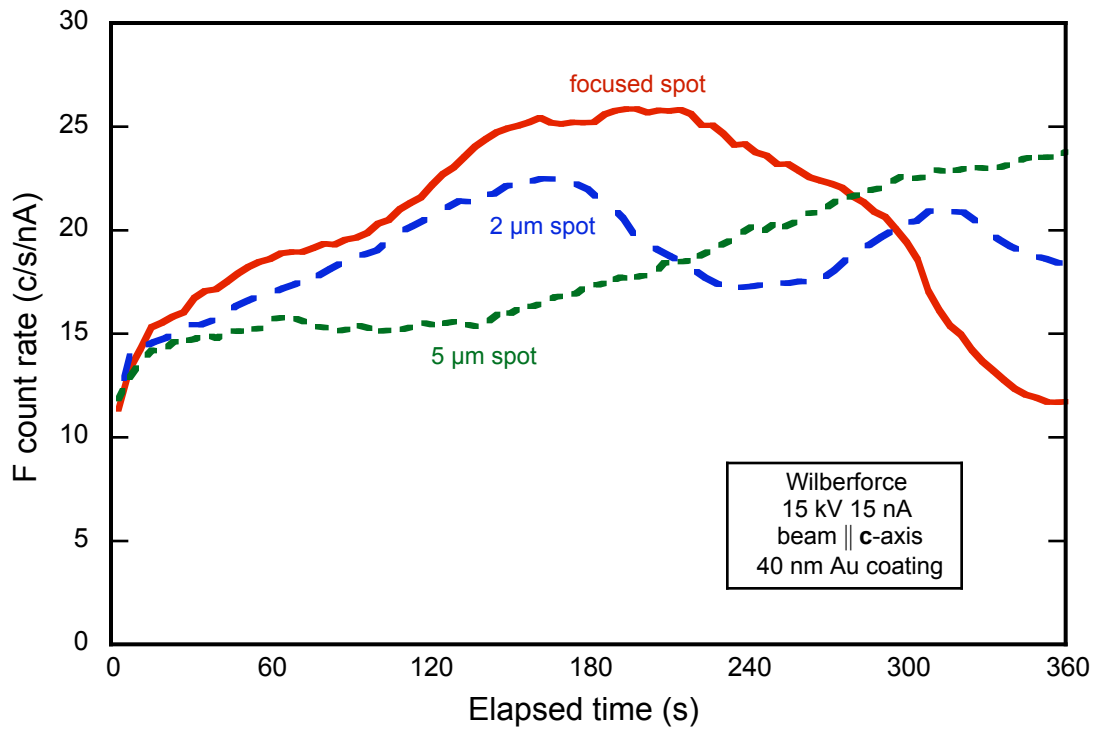


**Figure 17a.** F count rate with time on a section of Wilberforce apatite with the **c**-axis parallel to the beam coated with and coated with 40 nm of Au for several beam spot sizes at 15 kV and 15 nA.

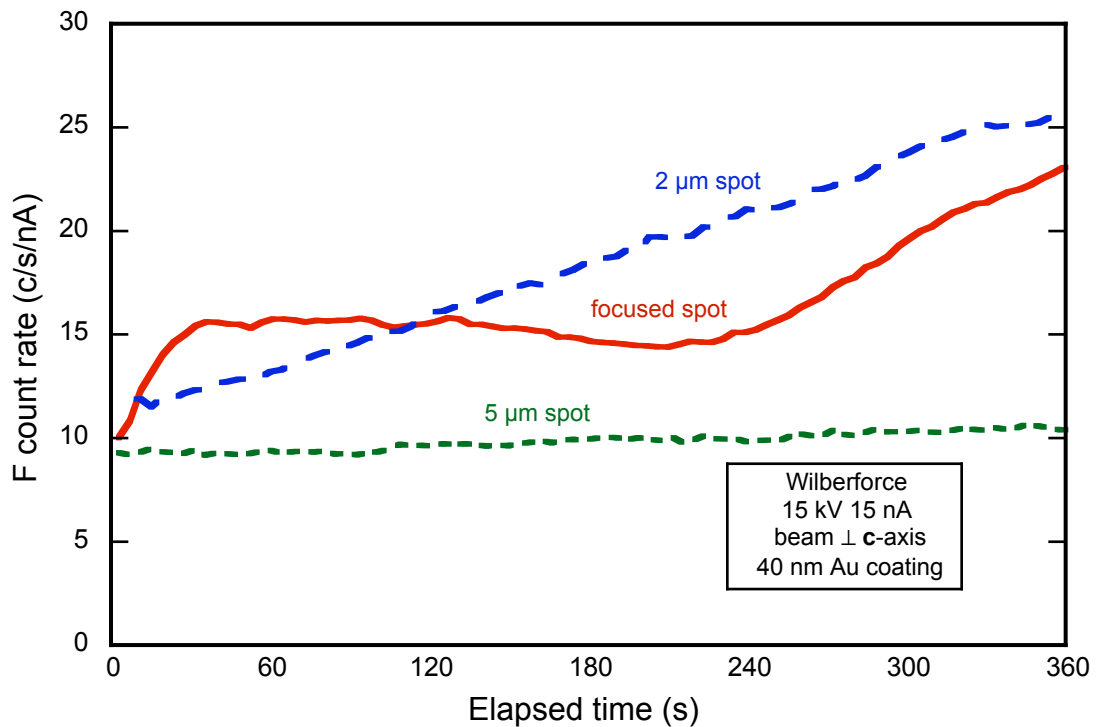


**Figure 17b.** F count rate with time on a section of Wilberforce apatite with the **c**-axis perpendicular to the beam and coated with 40 nm of Au for several beam spot sizes at 15 kV and 15 nA.

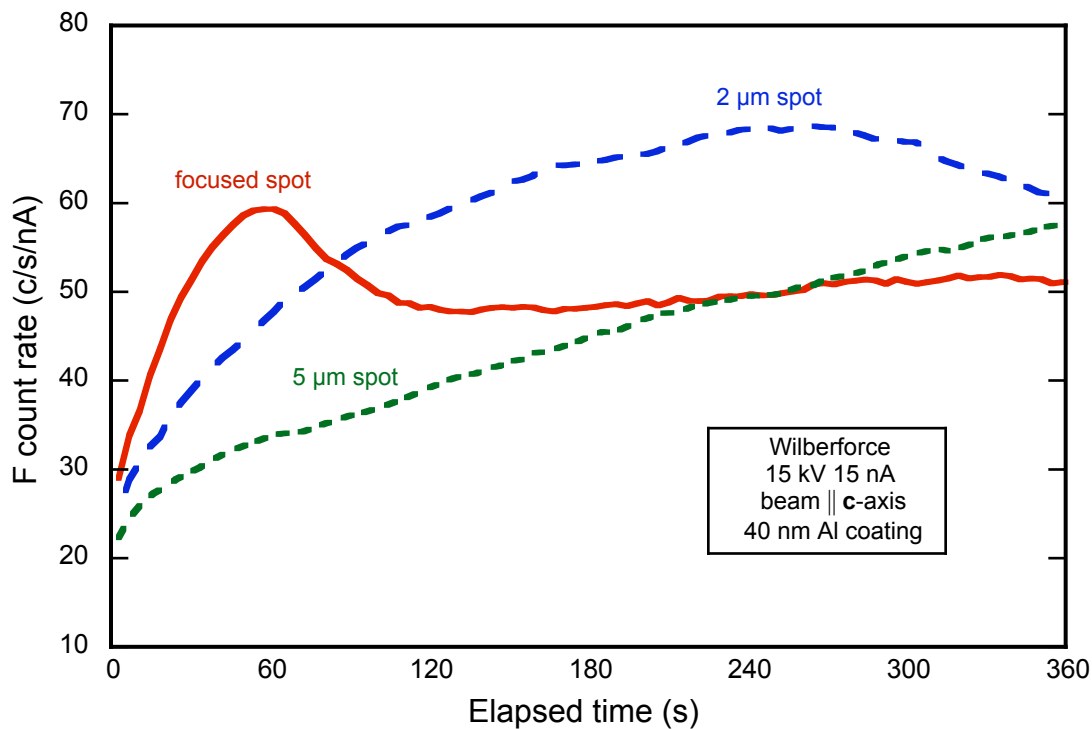


**Figure 18a.** F count rate with time on a section of Wilberforce apatite with the **c**-axis parallel to the beam and coated with 40 nm of Al for several beam spot sizes at 15 kV and 15 nA.

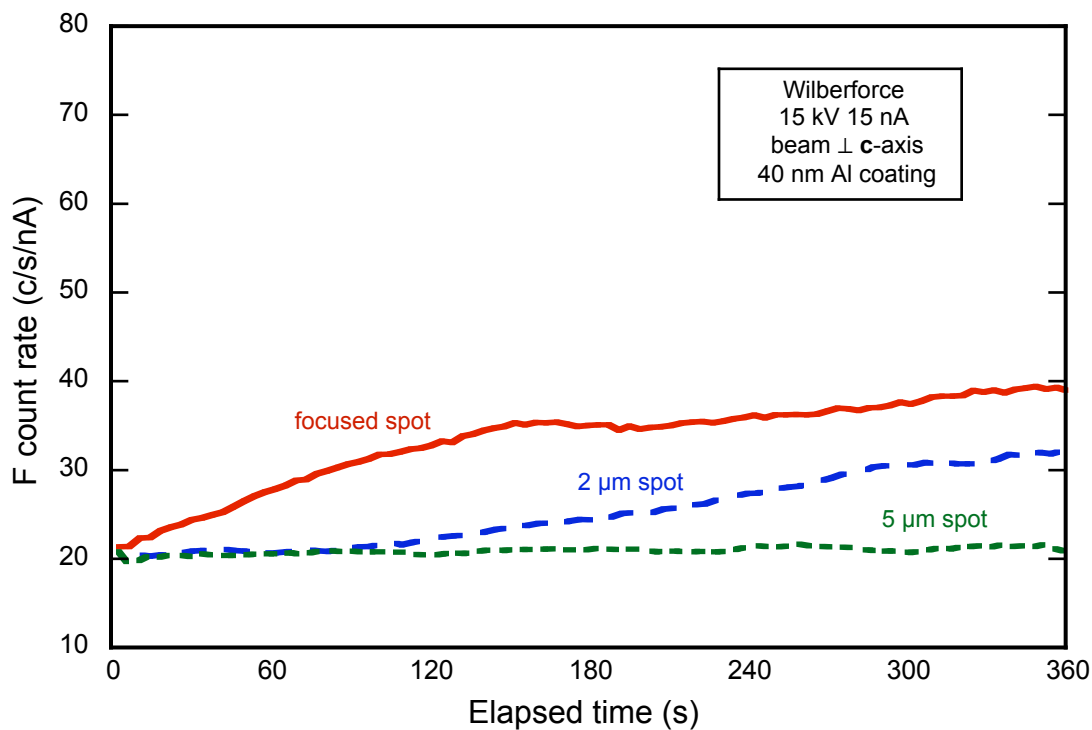


**Figure 18b.** F count rate with time on a section of Wilberforce apatite with the **c**-axis perpendicular to the beam and coated with 40 nm of Al for several beam spot sizes at 15 kV and 15 nA.

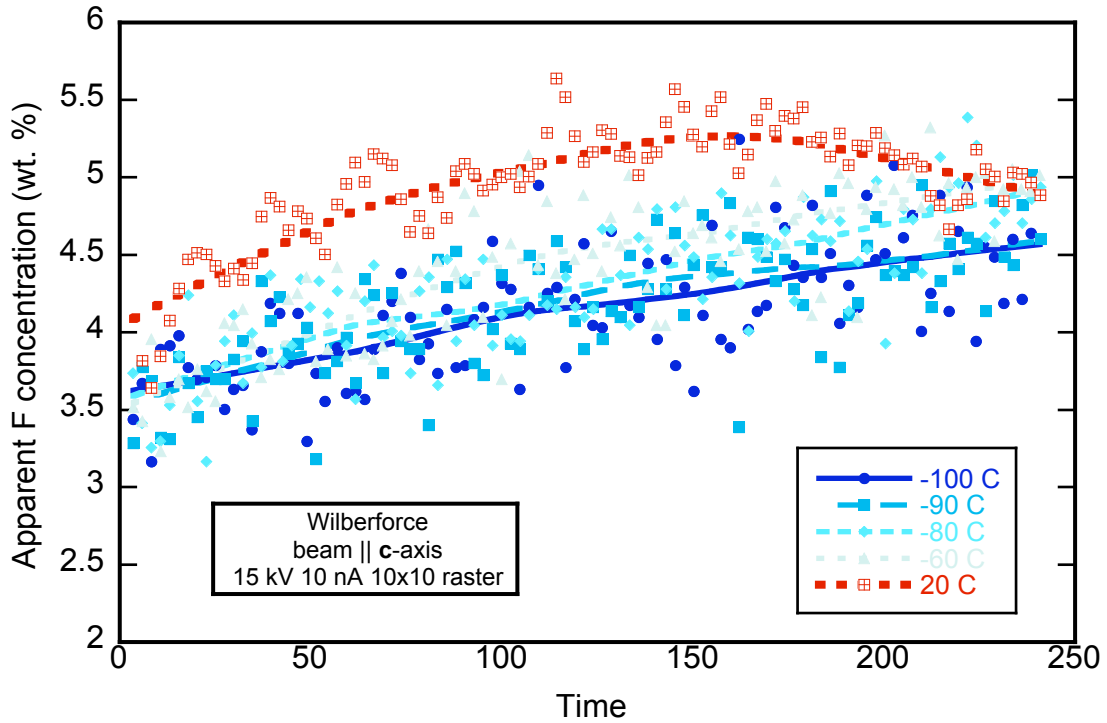


**Figure 19a.** Apparent F concentration with time on a section of Wilberforce apatite with the **c**-axis parallel to the beam at several temperatures. Nominal composition is 3.74 wt. % F.

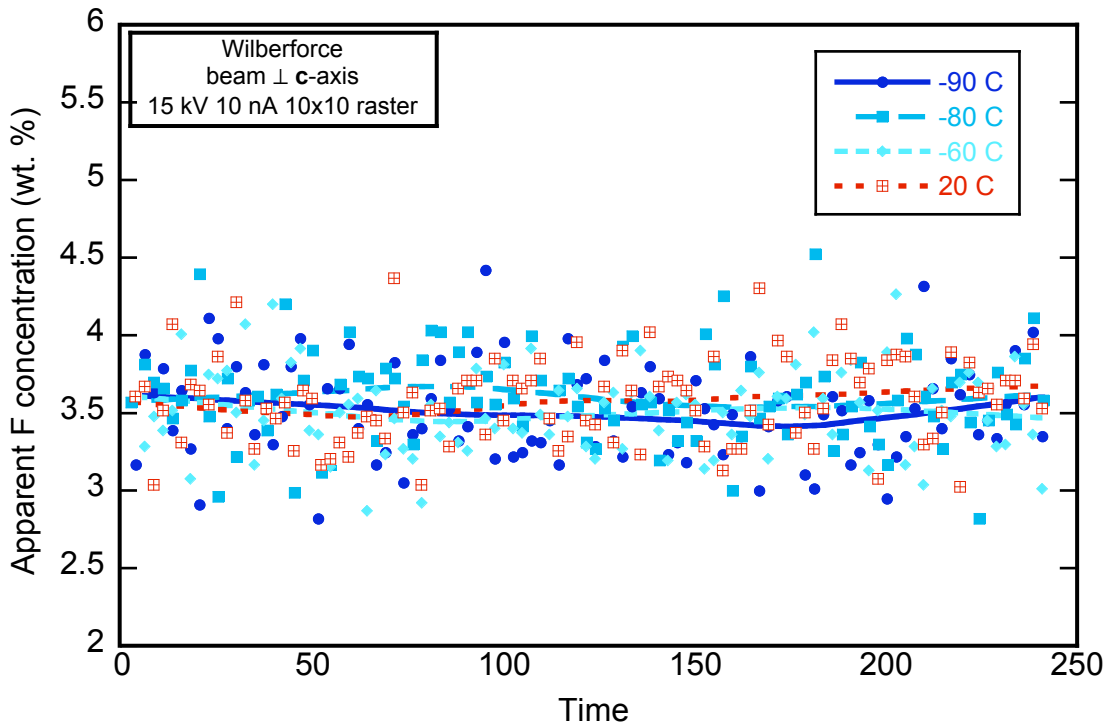


**Figure 19b.** Apparent F concentration with time on a section of Wilberforce apatite with the **c**-axis perpendicular to the beam at several temperatures. Nominal composition is 3.74 wt. % F.

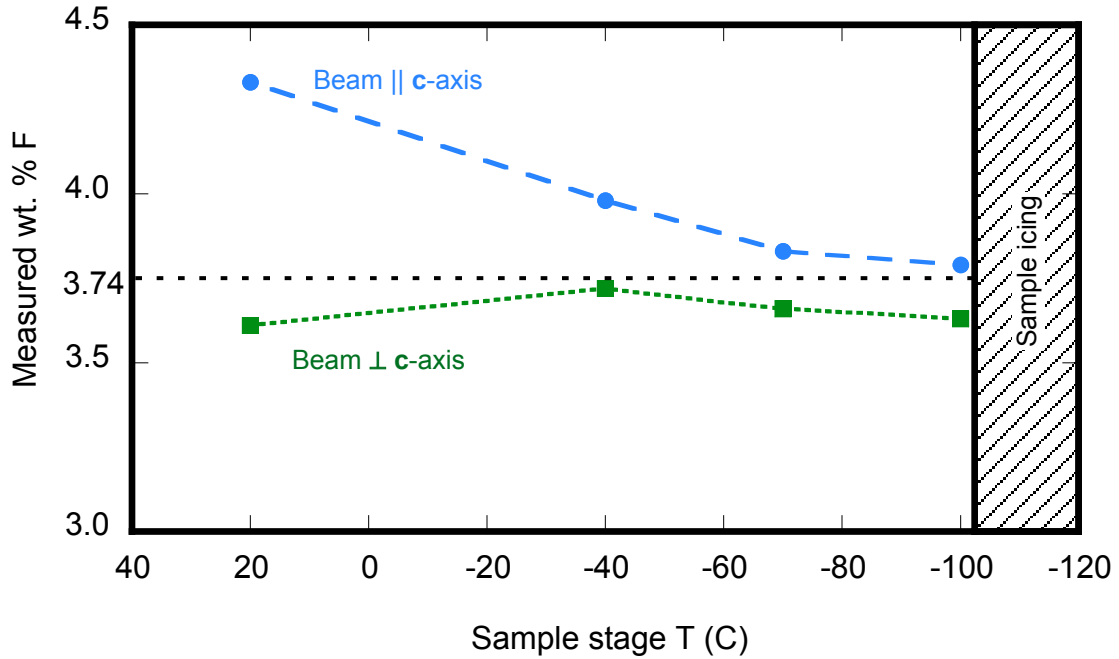


**Figure 20.** Measured F concentrations for Wilberforce apatite at several temperatures for two crystallographic orientations.. A zero time correction was used during analysis.

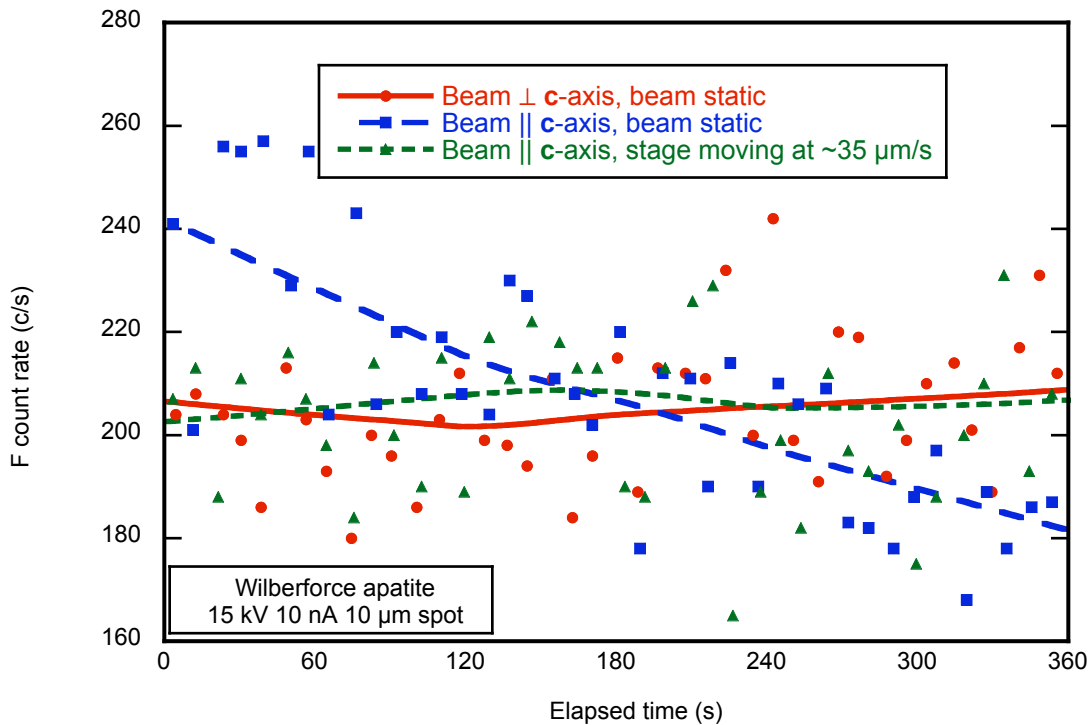


**Figure 21.** F count rate with time measured on Wilberforce apatite showing extrapolation to zero time for static and moving samples.

**Table 1.** Composition in weight percent of apatites analyzed by electron microprobe analysis.

<b>Sample</b>	<b>Gem3</b>	<b>SCM</b>	<b>HAM</b>	<b>Wilberforce</b>	<b>Durango</b>
<i># of analyses</i>	<i>19</i>	<i>19</i>	<i>18</i>	<i>19</i>	<i>20</i>
P <sub>2</sub> O <sub>5</sub>	40.88(68)	41.27(68)	40.72(68)	41.10(68)	41.04(68)
As <sub>2</sub> O <sub>5</sub>	0.02(2)	0.00(2)	0.01(2)	0.01(2)	0.08(2)
V <sub>2</sub> O <sub>5</sub>	0.01(1)	0.00(0)	0.00(1)	0.00(1)	0.01(1)
SO <sub>3</sub>	1.18(4)	0.10(3)	0.46(4)	0.38(4)	0.44(4)
SiO <sub>2</sub>	0.35(2)	0.14(2)	0.62(2)	0.12(2)	0.32(2)
Al <sub>2</sub> O <sub>3</sub>	0.00(1)	0.00(2)	0.00(1)	0.00(1)	0.00(1)
FeO	0.00(1)	0.04(1)	0.02(1)	0.01(1)	0.04(1)
CaO	54.79(54)	54.46(53)	54.95(54)	54.69(54)	54.22(53)
MgO	0.00(1)	0.01(1)	0.00(1)	0.01(1)	0.02(1)
MnO	0.01(1)	0.04(1)	0.00(1)	0.01(1)	0.00(1)
PbO	0.00(3)	0.00(3)	0.00(3)	0.00(3)	0.00(3)
BaO	0.01(2)	0.00(2)	0.00(2)	0.01(2)	0.00(2)
SrO	0.15(1)	0.20(1)	0.13(1)	0.53(1)	0.09(1)
Na <sub>2</sub> O	0.38(2)	0.27(2)	0.10(2)	0.28(2)	0.28(2)
K <sub>2</sub> O	0.00(1)	0.01(1)	0.00(1)	0.00(1)	0.00(1)
Y <sub>2</sub> O <sub>3</sub>	0.03(1)	0.27(2)	0.05(1)	0.05(1)	0.09(1)
La <sub>2</sub> O <sub>3</sub>	0.09(2)	0.19(2)	0.25(2)	0.18(2)	0.43(2)
Ce <sub>2</sub> O <sub>3</sub>	0.17(2)	0.41(2)	0.36(2)	0.39(2)	0.62(2)
Pr <sub>2</sub> O <sub>3</sub>	0.01(3)	0.04(3)	0.02(3)	0.04(3)	0.05(3)
Nd <sub>2</sub> O <sub>3</sub>	0.05(2)	0.23(2)	0.11(2)	0.18(2)	0.18(2)
Sm <sub>2</sub> O <sub>3</sub>	0.00(3)	0.05(3)	0.03(3)	0.04(3)	0.00(3)
Gd <sub>2</sub> O <sub>3</sub>	0.00(3)	0.06(3)	0.02(3)	0.01(3)	0.02(3)
Dy <sub>2</sub> O <sub>3</sub>	0.01(2)	0.06(2)	0.01(2)	0.02(2)	0.02(2)
ThO <sub>2</sub>	0.00(3)	0.00(3)	0.00(3)	0.00(3)	0.00(3)
<i>ΣREE Oxide</i>	<i>0.34</i>	<i>1.04</i>	<i>0.79</i>	<i>0.85</i>	<i>1.33</i>
UO <sub>2</sub>	0.00(4)	0.00(4)	0.00(4)	0.00(4)	0.00(4)
F	3.11(8)	4.05(10)	2.51(8)	3.74(10)	3.40(9)
Cl	0.01(2)	0.00(2)	0.33(2)	0.00(2)	0.46(2)
<i>H<sub>2</sub>O calc</i>	<i>0.31</i>	<i>0.00</i>	<i>0.51</i>	<i>0.02</i>	<i>0.05</i>
<i>CO<sub>2</sub> calc</i>	<i>0.00</i>	<i>0.65</i>	<i>0.00</i>	<i>0.00</i>	<i>0.00</i>
<i>-O=F,Cl</i>	<i>-1.31</i>	<i>-1.706</i>	<i>-1.13</i>	<i>-1.578</i>	<i>-1.535</i>
<i>Total</i>	<i>100.26</i>	<i>100.838</i>	<i>100.072</i>	<i>100.24</i>	<i>100.35</i>
<i>X<sub>F</sub></i>	<i>0.824</i>	<i>1.000</i>	<i>0.668</i>	<i>0.990</i>	<i>0.907</i>
<i>X<sub>Cl</sub></i>	<i>0.002</i>	<i>0.000</i>	<i>0.048</i>	<i>0.000</i>	<i>0.066</i>
<i>X<sub>OH</sub></i>	<i>0.174</i>	<i>0.000</i>	<i>0.284</i>	<i>0.009</i>	<i>0.028</i>
<i>O calc.</i>	<i>38.72</i>	<i>38.03</i>	<i>38.73</i>	<i>37.80</i>	<i>37.89</i>
O meas.	38.81(83)	38.69(79)	39.39(83)	38.41(80)	38.75(81)
<i>H<sub>2</sub>O calc</i>	<i>0.31</i>	<i>0.00</i>	<i>0.51</i>	<i>0.04</i>	<i>0.05</i>
H <sub>2</sub> O by IR/ERD	0.58	0.04 (IR only)	0.44	0.10 (IR only)	0.09

*Notes:* Crystallographic c-axis is perpendicular to the electron beam.. Numbers in italics represent calculated values. Error is 3σ.

**Table 2.** Structural formulae for the apatite compositions in Table 1.

<b>Sample</b>	<b>Gem3</b>	<b>SCM</b>	<b>HAM</b>	<b>Wilberforce</b>	<b>Durango</b>
P	2.90	2.93	2.90	2.91	2.93
As	0.00	0.00	0.00	0.00	0.00
V	0.00	0.00	0.00	0.00	0.00
S	0.07	0.01	0.03	0.02	0.03
Si	0.03	0.01	0.05	0.01	0.03
<b>Z site</b>	<b>3.00</b>	<b>2.95</b>	<b>2.98</b>	<b>2.94</b>	<b>2.99</b>
Al	0.00	0.00	0.00	0.00	0.00
Fe	0.00	0.00	0.00	0.00	0.00
Ca	4.92	4.90	4.95	4.90	4.90
Mg	0.00	0.00	0.00	0.00	0.00
Mn	0.00	0.00	0.00	0.00	0.00
Pb	0.00	0.00	0.00	0.00	0.00
Ba	0.00	0.00	0.00	0.00	0.00
Sr	0.01	0.01	0.01	0.03	0.00
Na	0.06	0.04	0.02	0.05	0.05
K	0.00	0.00	0.00	0.00	0.00
Y	0.00	0.01	0.00	0.00	0.00
La	0.00	0.01	0.01	0.01	0.01
Ce	0.01	0.01	0.01	0.01	0.02
Pr	0.00	0.00	0.00	0.00	0.00
Nd	0.00	0.01	0.00	0.01	0.01
Sm	0.00	0.00	0.00	0.00	0.00
Gd	0.00	0.00	0.00	0.00	0.00
Dy	0.00	0.00	0.00	0.00	0.00
<i>ΣREE</i>	<i>0.01</i>	<i>0.03</i>	<i>0.02</i>	<i>0.03</i>	<i>0.04</i>
Th	0.00	0.00	0.00	0.00	0.00
U	0.00	0.00	0.00	0.00	0.00
<b>M site</b>	<b>5.00</b>	<b>5.00</b>	<b>5.00</b>	<b>5.00</b>	<b>5.00</b>
F	0.82	1.07	0.67	0.99	0.91
Cl	0.00	0.00	0.05	0.00	0.07
<i>H (calc.)</i>	<i>0.17</i>		<i>0.28</i>	<i>0.01</i>	<i>0.03</i>
<i>C (calc.)</i>		<i>0.07</i>			

*Notes:* Normalization is to five M-site cations.

**Table 3.** Comparison of measured F concentrations (wt. %) from different sample orientations.

<b>Sample</b>	<b>Gem3</b>	<b>SCM</b>	<b>HAM</b>	<b>Wilberforce</b>	<b>Durango</b>
Beam perpendicular to <b>c</b> -axis	3.11(8)	4.05(10)	2.51(8)	3.74(10)	3.40(9)
Beam parallel to <b>c</b> -axis	3.13(12)	4.33(13)	2.53(11)	4.08(12)	3.82(20)

*Notes:* Measurements acquired with zero time correction with at 15 kV, 10 nA, 10  $\mu$ m diameter beam.  
Error is 3s.



**Table 4.** Apatite compositions determined by EMPA compared with literature values.

Sample <i>Source</i>	Durango		Wilberforce			
	EMPA (3σ)	<i>Young et al. 1969</i>	EMPA (3σ)	<i>USGS 1972*</i>	<i>Loomis (wet)</i>	<i>Evans (EMPA)</i>
P <sub>2</sub> O <sub>5</sub>	41.04(68)	40.78	41.10(68)	40.93	40.71	
As <sub>2</sub> O <sub>5</sub>	0.08(2)	0.09	0.01(2)			
V <sub>2</sub> O <sub>5</sub>	0.01(1)	0.01	0.00(1)			
SO <sub>3</sub>	0.44(4)	0.37	0.38(4)	0.59		0.60
CO <sub>2</sub>		0.05				
SiO <sub>2</sub>	0.32(2)	0.34	0.12(2)	0.11	0.25	0.13
Al <sub>2</sub> O <sub>3</sub>	0.00(1)	0.07	0.00(1)			0.02
FeO	0.04(1)	0.00	0.01(1)			
Fe <sub>2</sub> O <sub>3</sub>		0.06		0.04	0.06	0.03
CaO	54.22(53)	54.02	54.69(54)	54.31	54.94**	
MgO	0.02(1)	0.01	0.01(1)	0.01		
MnO	0.00(1)	0.01	0.01(1)		0.03	0.02
SrO	0.09(1)	0.07	0.53(1)	0.23		
Na <sub>2</sub> O	0.28(2)	0.23	0.28(2)	0.24	0.24	
K <sub>2</sub> O	0.00(1)	0.01	0.00(1)			
Y <sub>2</sub> O <sub>3</sub>	0.09(1)		0.05(1)	0.04		
La <sub>2</sub> O <sub>3</sub>	0.43(2)		0.18(2)	0.13		
Ce <sub>2</sub> O <sub>3</sub>	0.62(2)		0.39(2)	0.29		
Pr <sub>2</sub> O <sub>3</sub>	0.05(3)		0.04(3)	0.04		
Nd <sub>2</sub> O <sub>3</sub>	0.18(2)		0.18(2)	0.12		
Sm <sub>2</sub> O <sub>3</sub>	0.00(3)		0.04(3)	0.02		
Gd <sub>2</sub> O <sub>3</sub>	0.02(3)		0.01(3)	0.01		
Dy <sub>2</sub> O <sub>3</sub>	0.02(2)		0.02(2)	0.001		
ΣREE Oxide	1.33	1.43	0.85	0.61		
ThO <sub>2</sub>	0.00(3)	0.02	0.00(3)			
F	3.40(9)	3.53	3.74(10)	3.67	3.40	3.85***
Cl	0.46(2)	0.41	0.00(2)		0.05	<0.02
-O = F,Cl	-1.54	-1.59	-1.58	-1.59		
H <sub>2</sub> O calc.	0.05		0.04			
H <sub>2</sub> O <sup>+</sup>		0.01		0.03	0.02	
H <sub>2</sub> O <sup>-</sup>					0.005	
Total	100.35	99.93	100.24	99.83	99.70	

*Notes:* \*Also noted as "Beeson apatite" as measured by analyst S.T. Neil, with N.H. Suhr, M. Cremer, L.B. Schlocker, and H.N. Elsheimer. \*\*Includes SrO. \*\*\* Radioactivation analysis (±0.15%) by H.A. Vincent.

**Table 5.** Comparison of compositions of synthetic apatites in weight percent as measured by EMPA and by wet chemistry.

<b>Sample</b>		<b>25</b>	<b>21</b>	<b>18</b>	<b>17</b>	<b>36</b>	<b>29</b>	<b>26</b>
<b>F</b>	EMPA (MgF2)	3.71(8)	3.22(8)	2.72(7)	1.99(6)	1.27(5)	0.67(4)	0.04(3)
	EMPA (fluortopaz)	3.89(10)	3.44(9)	2.77(8)	2.06(7)	1.27(6)	0.72(5)	0.09(3)
	Wet	3.77	3.32(7)	2.74(7)	2.05(13)	1.37(5)	0.58(4)	0.01
<b>Cl</b>	EMPA	0.00(1)	0.76(2)	1.65(4)	2.82(9)	4.24(13)	5.08(10)	6.43(12)
	Wet	0.01(8)	0.77(3)	1.86(6)	2.78(7)	4.59(26)	5.17(9)	6.44(10)
<b>Ca</b>	EMPA	39.22(13)	39.16(20)	39.13(13)	38.79(13)	38.46(13)	38.48(13)	38.28(13)
	Wet	39.12(68)	39.34(31)	38.94(18)	38.63(16)	38.91(10)	38.46(30)	38.07(32)
<b>P</b>	EMPA	18.49(17)	18.45(17)	18.35(17)	18.23(17)	18.07(17)	18.02(17)	17.86(17)
	Wet	18.12(38)	18.29(17)	18.16(8)	17.91(1)	17.91(7)	18.00(8)	17.70(14)
<b>O</b>	EMPA (direct analysis)	38.54(68)	38.53(68)	38.62(68)	38.37(68)	38.09(68)	38.34(68)	37.65(67)
	Wet	37.43	37.78	37.53	37.01	37.02	36.70	36.56
	EMPA:Wet	1.03	1.02	1.03	1.04	1.03	1.04	1.03
<b>Total</b>	EMPA	99.96	100.12	100.47	100.22	100.31	100.59	100.27
	Wet	98.45	99.50	99.23	98.38	99.62	98.67	98.78

*Notes:* Synthetic apatites described by Schettler et al. (2011). EMPA F results are shown for two different calibration standards (see text). The EMPA results are an average of 10 separate analysis points. Error is  $2\sigma$ .

**Table 6.** Apatite measured F concentrations (wt. %) as a function of sample temperature.

<b>Beam size</b>	<b>T (C)</b>	<b>Durango</b>	<b>Wilberforce</b>	<b>Gem3f</b>	<b>HAM</b>
Focused spot	20	3.25(36)	4.93(70)	3.98(76)	3.18(20)
	-90	3.2822)	4.26(49)	3.44(29)	2.89(50)
3 $\mu\text{m}$ x 3 $\mu\text{m}$ raster	20	3.37(18)	4.04(35)	3.47(10)	2.56(33)
	-90	3.33(25)	3.69(39)	2.91(24)	2.47(36)
6 $\mu\text{m}$ x 6 $\mu\text{m}$ raster	20	3.41(12)	3.82(19)	3.03(13)	2.39(11)
<b>Nominal composition</b>		<b>3.40</b>	<b>3.74</b>	<b>3.11</b>	<b>2.51</b>

*Notes:* Zero time correction used with a beam condition of 15 kV and 10 nA. Samples oriented with **c**-axis parallel to electron beam. Each analysis represents an average of three points at 20 C and 5 points at -90 C. Error is  $2\sigma$ .

**Table 7.** Effect of stage motion on measured F concentration.

<b>Orientation</b>	<b>Speed</b>	<b>Wilberforce</b>	<b>Durango</b>	<b>SCM</b>
⊥ <b>c-axis</b>	static	3.75(12)	3.37(12)	4.05(13)
⊥ <b>c-axis</b>	~35 μm/s	3.73(7)	3.42(6)	3.95(6)
<b>c-axis</b>	static	4.08(12)	3.82(12)	4.33(13)
<b>c-axis</b>	~4 μm/s	3.88(7)	3.48(6)	4.01(6)
<b>c-axis</b>	~35 μm/s	3.81(7)	3.39(6)	3.80(7)
<b>c-axis</b>	~75 μm/s	3.81(7)	--	--
<b>Nominal wt. % F</b>		3.74	3.40	4.05

*Notes:* Electron beam was set to 15 kV, 10 nA and 10 μm diameter. A zero time correction was used for the static beam analyses. The listed values represent an average of 10 analyses. Error is 3σ.